

AD-A164 912

DISCRIMINATION OF WATER FROM SHADOW REGIONS ON RADAR
IMAGERY USING COMPUTER VISION TECHNIQUES(U) MNEMONICS
INC SALINE MI J QIAN ET AL. SEP 85 ETL-8484

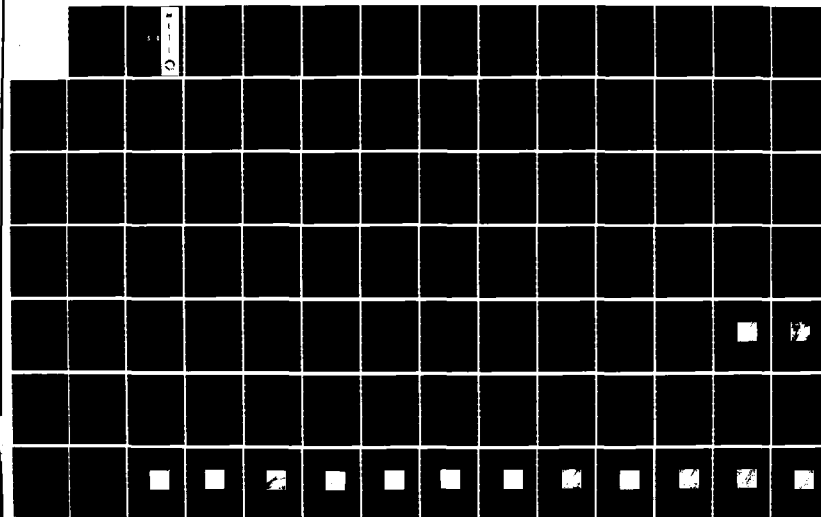
1/2

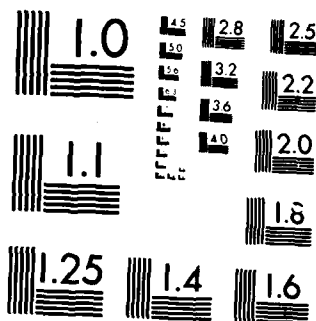
UNCLASSIFIED

DACRA76-84-C-0003

F/G 17/9

NL





MICROCOPY RESOLUTION TEST CHART
NATIONAL BUREAU OF STANDARDS 1963-A

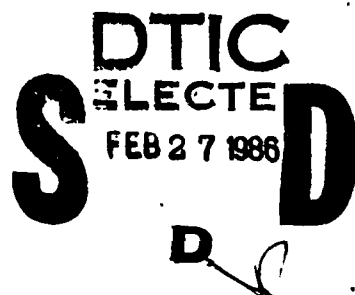
AD-A164 912

ETL - 0404

(2)

Discrimination of water from
shadow regions on radar
imagery using computer
vision techniques

Jianzhong Qian
Robert M. Haralick



Mnemonics, Inc.
Saline, Michigan 48176

FILE COPY
September 1985

APPROVED FOR PUBLIC RELEASE; DISTRIBUTION IS UNLIMITED.

Prepared for
U.S. ARMY CORPS OF ENGINEERS
ENGINEER TOPOGRAPHIC LABORATORIES
FORT BELVOIR, VIRGINIA 22060-5546

86 227 016



E

T

L

UNCLASSIFIED

SECURITY CLASSIFICATION OF THIS PAGE (When Data Entered)

REPORT DOCUMENTATION PAGE		READ INSTRUCTIONS BEFORE COMPLETING FORM
1. REPORT NUMBER ETL-0404	2. GOVT ACCESSION NO. AD1/64 912	3. RECIPIENT'S CATALOG NUMBER
4. TITLE (and Subtitle) DISCRIMINATION OF WATER FROM SHADOW REGIONS ON RADAR IMAGERY USING COMPUTER VISION TECHNIQUES		5. TYPE OF REPORT & PERIOD COVERED Final Technical Report March 1984 - July 1985
7. AUTHOR(s) Jianzhong Qian Robert M. Haralick		6. PERFORMING ORG. REPORT NUMBER DACA76-84-C-0003
9. PERFORMING ORGANIZATION NAME AND ADDRESS Mnemonics, Inc. Saline, Michigan 48176		10. PROGRAM ELEMENT, PROJECT, TASK AREA & WORK UNIT NUMBERS
11. CONTROLLING OFFICE NAME AND ADDRESS U.S. Army Engineer Topographic Laboratories Fort Belvoir, Virginia 22060-5546		12. REPORT DATE September 1985
		13. NUMBER OF PAGES 132
14. MONITORING AGENCY NAME & ADDRESS (if different from Controlling Office)		15. SECURITY CLASS. (of this report) Unclassified
		15a. DECLASSIFICATION/DOWNGRADING SCHEDULE
16. DISTRIBUTION STATEMENT (of this Report) Approved for public release; distribution is unlimited.		
17. DISTRIBUTION STATEMENT (of the abstract entered in Block 20, if different from Report)		
18. SUPPLEMENTARY NOTES		
19. KEY WORDS (Continue on reverse side if necessary and identify by block number) MTA filter SAR imagery Noise removal Scene analysis Radar interpretation Texture preserving		
20. ABSTRACT (Continue on reverse side if necessary and identify by block number) Unlike MSS LANDSAT imagery and other photography, the specific characteristics of the intensity of water and shadow in SAR imagery make the task of discriminating between them extremely difficult. In this report, we analyze the mechanism of reflectivity of water and shadow on radar imagery and describe a scene-analysis system which consists of a texture-preserving noise-removal procedure as the preprocessing step, a probabilistic relaxation algorithm to do the low-level labeling, and a spatial reasoning procedure based on a relational model to perform the high-level interpretation. The experimental results obtained from the SAR images are presented to illustrate the performance of this system.		

PREFACE

The work documented in this report was performed under contract DACA76-84-C-0003 for the U.S. Army Engineer Topographic Laboratories, Fort Belvoir, Virginia, by Mnemonics, Inc., Saline, Michigan. The Contracting Officer's Technical Representative was Dr. Frederick W. Rohde.

TABLE OF CONTENTS

I. INTRODUCTION	1
II. CHARACTERISTICS OF SHADOW AND WATER REGIONS ON SAR IMAGES	5
III. TEXTURE PRESERVING AND NOISE REMOVAL	10
IV. STATISTICAL LABELING AND ADAPTIVE RELAXATION	18
V. USING A RELATIONAL MODEL TO REDUCE AMBIGUITIES	31
VI. EXPERIMENTAL RESULTS	41
VII. CONCLUSIONS	127
REFERENCES	129

Accesion For	
NTIS	CRA&I
DTIC	TAB
Unannounced	
Justification	
By	
Distribution /	
Availability Codes	
Dist	Avail and/or Special
A-1	

LIST OF ILLUSTRATIONS

Figure 1. Block diagram of the system.	4
Figure 2. Principle of MTA filter	15
Figure 3. Relationship of the neighbor sets.	28
Figure 4. Relational graph model	34
Figure 5. Direction and order of searching	39
Figure 6. Test image 1	60
Figure 7. 64 level quantization of image 1	61
Figure 8. Histogram of image 1	62
Figure 9. Histogram of quantized image 1	63
Figure 10. Histogram of sampled water area	64
Figure 11. Histogam of sampled shadow area	65
Figure 12. Histogram of texture entropy (q)	66
Figure 13. Histogram of texture entropy (s)	67
Figure 14. Histogram of texture entropy (w)	68
Figure 15. Histogram of inverse difference moment(q) . .	69
Figure 16. Histogram of inverse difference moment (w)	70
Figure 17. Histogram of inverse different moment (s) .	71
Figure 18. Histogram of entropy (f1)	72
Figure 19. Histogram of entropy (f2)	73
Figure 20. Histogram of entropy (f3)	74
Figure 21. Histogram of inverse difference moment(f1)	75
Figure 22. Histogram of inverse difference moment(f2)	76
Figure 23. Histogram of inverse difference moment(f3)	77
Figure 24. Test image 2	78

Figure 25. GTCM texture image for image 2	79
Figure 26. Segmentation of image 2 (a)	80
Figure 27. Segmentation of image 2 (b)	81
Figure 28. Test image 3	82
Figure 29. Thresholding GTCM of image 3.	83
Figure 30. Bright linear features	84
Figure 31. Filtered result of image 1	85
Figure 32. Generalized gradient image (1)	86
Figure 33. Filtered result by different thresholds . .	87
Figure 34. Generalized gradient image (2)	88
Figure 35. Inverse difference moment image (1) . .	89
Figure 36. Inverse difference moment image (2) . .	90
Figure 37. Entropy image of image 1	91
Figure 38. Entropy of filtered image 1	92
Figure 39. Generalized gradient image (a)	93
Figure 40. Labeling result (a1)	94
Figure 41. Labeling result (a2)	95
Figure 42. Training sample set for image 1	96
Figure 43. Labeling result for image 1 (a)	97
Figure 44. Relaxation result for above image	98
Figure 45. The mean and covariances for figure 46 . .	99
Figure 46. Labeling result for image 1 (b)	100
Figure 47. Labeling result for image 1 (c)	101
Figure 48. Test image 4.	102
Figure 49. Quantized image 4	103
Figure 50. Entropy of image 4	104

Figure 51. Inverse different moment of image 4	105
Figure 52. Training sampling set for image 4	106
Figure 53. Labeling result for image 4 (a)	107
Figure 54. Labeling result for image 4 (b)	108
Figure 55. Labeling result for image 4 (c)	109
Figure 56. The mean and covariances for fig. 57	110
Figure 57. Labeling result for image 4 (d)	111
Figure 58. Relaxation result for fig. 57 (a)	112
Figure 59. Relaxation result for fig. 57 (b)	113
Figure 60. Labeling result for image 4 (e)	114
Figure 61. Initial labeling result	115
Figure 62. Ground truth map.	116
Figure 63. Comparison of error reduction.	117
Figure 64. Labeling result	118
Figure 65. New indexing symbolic image 1.	119
Figure 66. New indexing symbolic image 2.	120
Figure 67. Spatial reasoning result 1.	121
Figure 68. Spatial reasoning result 2.	122
Figure 69. Test image 5	123
Figure 70. Low level labeling of image 5	124
Figure 71. New indexing symbolic image 3	125
Figure 72. Spatial reasoning result 3	126

I INTRODUCTION

There has been little work done to automatically discriminate between water regions and shadow regions on a SAR radar image in an automated procedure. With the increasing need for analyzing large volumes of radar data by computer, however, this becomes an important recognition task.

In areas of high relief, an airborne SAR radar image creates many radar shadow regions which may be confused with the water regions, since both water and shadow regions appear dark and with subtle differences in tone and texture. This problem could be resolved by an additional flight line having an opposite look direction. The original shadowed regions in the new flight line would disappear, and the water regions would still remain dark. However, this solution is often impractical.

In this report we describe a scene analysis system which can discriminate between water and shadows by using contextual information. See Figure 1. The technique is based on understanding the radar reflectivity which is related to the size, shape and surface material of the terrain illuminated by the radar wave. First, the statistical textural feature extraction algorithm is used to extract significant features from the gray-tone co-occurrence matrices for discriminating water regions and shadow regions on the radar imagery. A

Maximum Likelihood Decision rule, which incorporates both tonal and textural features into the labeling process, and an adaptive probabilistic relaxation algorithm, which incorporates the contextual information into the labeling process, are then applied to obtain the initial labeling and to improve the labeling accuracy. Second, according to our prior knowledge of the water regions and shadow regions on SAR imagery, a relational model is constructed and several structural contextual features are measured to create the symbolic description. Then a spatial reasoning process using a set of structural decision rules is invoked. Finally, a new interpreted symbolic image is generated in which the specified objects (shadows and water) are clearly identified. Before doing that, some preprocessing such as requantization and texture preserving noise removal may be applied to enhance the useful features.

A set of SAR images collected over Huntsville, Alabama on 17 June, 1977 and another set collected over the Elizabeth City area on 10 October, 1980 have been processed using this system. The experiments performed show that the two level combination discriminating algorithm can provide significant capability for discriminating the water regions from the shadow regions. Because of the use of contextual information, the probabilistic labeling relaxation improved the labeling result on the pixel level, and the spatial reasoning method reduced ambiguities on the region level. From the final re-

sults of three test images, we can see that most of water regions and shadow regions are identified correctly. We will discuss these results in detail in Chapter VI.

INPUT IMAGE

PREPROCESSING

USING A CONTEXTUAL DEPENDENT MAT FILTER
FOR TEXTURE PRESERVING NOISE REMOVAL

FEATURE EXTRACTION

USING STATISTICAL GCMT MEASURING
BASED ON TEXTURE AND GRAY TONE INFORMATION

LOW LEVEL LABELING

USING ADAPTIVE PROBABILISTIC RELAXATION
BASED ON PIXEL LEVEL CONTEXTUAL INFORMATION

SYMBOLIC DESCRIPTION

DEPTH FIRST REGION ATTRIBUTES MEASURING
BASED ON REGION LEVEL CONTEXTUAL INFORMATION

OBJECT INTERPRETATION

USING SPATIAL REASONING
BASED ON A RELATIONAL MODEL AND A STRUCTURE
DECISION RULE

OUTPUT RESULT

Figure 1. Block diagram of the system.

II CHARACTERISTICS OF SHADOW AND WATER REGIONS ON SAR IMAGES

Most of the practical knowledge of radar interpretation has been derived from studies of radar images including the comparison and correlation with ground truth information and aerial photography.

The differences of tones and textures between water and shadow regions on SAR imagery are depend on the different ground situations. However, these differences are subtle.

In flat terrain area, low returns are received from surfaces acting as specular reflectors having surface roughness much less than the wavelength of the radar(less than $\lambda/10$). Examples are: water, pavements and dry lakebeds. Therefore, the gray tone values of water region on radar imagery are relatively low and appear pretty dark. When the wind is still and water is flat, quiet-water surfaces are near perfect specular reflectors. In this case, the return signal will be almost zero. As a result, the gray tone in these regions is completely black. It is just like that in ideal shadow regions on SAR imagery.

Textures of water regions on SAR imagery usually are created by following two factors.

In the open water areas which are either standing or flowing water bodies without vegetation covering them, the

surface agitated by wind backscatters a strong radar return which can be called the "sea return" [1]. The tonal and textural differences of the open water area on the SAR imagery may indicate some surface wave action. Here the gray tones corresponding to the wavey water surface form the texture of the water region.

Also, there is the case of the floating and standing vegetation which may cover or partially cover the surface of water bodies. This makes the situation more complex, since signals returned from this vegetation may be quite varied. This creates another kind of texture in water regions. It has been observed that the darker the return on the imagery, the greater the amount of open water relative to the vegetation [2].

On the other hand, the tones and textures in shadow regions on SAR imagery are caused by following factors. When a bright return occurs from hill slopes or high objects facing the radar look direction, a shadowed region on the far sides of the crests follows, since there is no signal returned from the occluded part of the terrain. Unlike shadows in aerial photography which are weakly illuminated by energy scattered by atmosphere, the radar shadow is completely black and sharply defined. If there is no noise, then an ideal shadow region on SAR imagery should not have any texture. Another case, however, should be considered. If the aircraft

reaches a position such that the farther side of slope of the mountain is no longer behind the crests, instead of the totally black shadow, a very weak signal from the slope faced away from radar will return. The corresponding parts in the radar image appear relatively dark; we also can view them as shadows. It should be noted that an intermediate case may occur between the above two situations so that the shadow appears partially black and partially relatively dark. This causes variable texture patterns so that it is difficult to separate it from that of water regions.

Moreover, shadows can also occur on the water surface when the waves are significantly high. While the tops of the crests facing the radar look direction yield the strongest signal return, the absence of signals is from the far slopes of waves. However, these shadow regions are small and are within the water area. We consider the waves as the parts of a water body, so they should be eliminated or merged into the water regions.

Besides the above tonal and textural information, there are several structural features which are very helpful for discriminating between water and shadows on SAR imagery. The first thing is a complex signal return case known as the "cardinal effect". This is a result caused by a corner reflector formed by the combinations of two flat surfaces at right angle to one another. These adjacent smooth surfaces

cause a double reflection that yields very bright "speckles" or lines on the SAR imagery.

Another useful structural feature exists on water body boundaries on SAR imagery, known as the "Far shore brightening effect". This is caused by the smooth water area with a higher beach which is facing the radar look direction. Since this feature usually covers only small areas of the scene, they often appear as bright lines on SAR imagery. For this case, the dark area comes first, following a bright linear feature which is nearly normal to the radar look direction.

Because the oblique illumination of SAR produces strong returns from the sides of ridges and peaks facing the radar antenna, this makes the boundary appear very bright between shadow and shadow making objects where the near range area of the boundary is not flat. In most cases, these bright linear features are oriented normal or nearly normal to the radar look direction. That is, the bright linear feature comes first, and the dark region follows along the radar look direction. This situation is just the opposite to that of a water body boundary.

Another property of shadows in SAR image is that the radar illumination becomes more oblique in the far range direction and shadows are proportionally longer. This is different from the constant elevation angle of solar illumination in an aerial photograph. However, the shadow length along the radar

look direction is limited to a certain value for a given image, since the height of shadow-making objects is relatively small compared to the flying height of the airplane.

From the above analysis, we can see that there are some tonal and textural features which are useful for discriminating water and shadows on radar imagery. In some cases, however, these may not be enough. There are also several structural contextual dependency features. This structural information can be also incorporated into an automated radar image processing scheme. The remainder of the report discusses these issues.

III TEXTURE PRESERVING AND NOISE REMOVAL

Because both water regions and shadow regions in radar images are not rich in texture, the noise will tend to mask whatever texture there is and make the recognition task more difficult. Noise in radar imagery can come from two sources. One is radar coherent speckle noise[3], the other is quantization noise. We need to remove this noise while preserving the weak texture and other subtle detail information. This kind of noise removal is different from the kind which also smooths the weak texture in the filtering process.

Unfortunately, most filtering techniques tend to wash out the weak textures that we want to use. For example, the SFILT which we developed before is based on Lee's refined local statistics method which removes the noise along edges according to eight different kinds of edges. It was pointed out that this method created artifacts, because it used the directional masks in the filtering process [4]. Our experiments confirm that it preserved the sharp edges well, but it washed out detailed texture information. In fact, the SFILT only used a weighted average method in which the weights were determined by one directional gradient. The multi-threshold adaptive MTA filtering which is described in this section uses different filtering methods according to the local activity that is measured by a generalized gradient function.

There is a compromise between noise removal and texture preservation. Usually a filter which has powerful noise cleaning capability may remove or spatially distort edge, line and texture information. In contrast, a filter which preserves subtle detail will tend to have low noise cleaning capability. Spatial filters attempt to balance the information preserving requirement with the noise cleaning requirement. However, the balance is often done in a one-dimensional way. For example, a mean filter is good only for an image which consists of large homogeneous regions, while a median filter is only good for an image rich in sharp edges and some impulse noise. Some other weighted averaging filters may be good for a case between the above two extreme situations. are problem oriented. A real world image consists of many regions in which local activity varies from region to region. It is difficult for a filter optimized for one kind of condition to work well in another. Based on this consideration, it is appropriate to design a method in which several simple filters can be combined to form a more efficient and more flexible context dependent filter. Thus the advantages of each can be preserved, and their drawbacks can be avoided to get an optimal effect.

In this section, we describe a gradient oriented multi-threshold adaptive filtering technique for the purpose of cleaning noise and preserving texture. The regions of an image differ in their local texture and their contrast. There-

fore, they need different filtering algorithms to balance the noise removal against the texture preservation. The filtering that we discuss is region dependent. It uses a generalized gradient function which reflects the local contextual information as a cue to determine the nature of the filtering for each local neighborhood.

The algorithm is as follows:

(1) First, a generalized gradient function for every pixel is computed.

Let Z_{ij} be the pixel gray tone value to be filtered and G_{ij} be the corresponding local generalized gradient function within a $N \times N$ window. In order to avoid the effects of random noise in computing G_{ij} , we use the local gray tone submean M_{kd} instead of individual pixel value. If it is assumed that the size of any noise random cluster is three or fewer pixels, then the above consideration is sufficient.

Let Z_{sr} be a set of neighbors of pixel(i,j) having gray tone intensity Z_{ij} . The gray tone submeans are given by

$$M_{ij} = \sum_{s=q}^f \sum_{r=p}^g Z_{sr} \quad (4.1)$$

where

$$g = i - [(N-1) / 2 - 2(k-1)]$$

$$f = i - [d-2(k-1)]$$

$$p = j - [(N-1) / 2 - 2(d-1)]$$

$$q = j - [d - 2(k-1)]$$

and where $k, d = 1, 2, \dots, (N - 1)/2$.

Then for the four directions, the local gradients G_s 's are

$$G_s^0 = | (M_{11} + M_{12} + M_{13}) - (M_{31} + M_{32} + M_{33}) | \quad (4.2)$$

$$G_s^{\pi/4} = | (M_{11} + M_{12} + M_{21}) - (M_{32} + M_{33} + M_{23}) | \quad (4.3)$$

$$G_s^{\pi/2} = | (M_{11} + M_{21} + M_{31}) - (M_{13} + M_{23} + M_{33}) | \quad (4.4)$$

$$G_s^{3\pi/4} = | (M_{12} + M_{13} + M_{23}) - (M_{31} + M_{32} + M_{21}) | \quad (4.5)$$

and the final gradient is proportional to the sum of the directional gradients

$$G_{ij} = C \sum_{n=0}^3 G_s^{n\pi/4} \quad (4.6)$$

where C is the scaling factor.

The resulting G_{ij} is a good measure of the local texture contrast.

(2). A set of thresholds can then be applied to G_{ij} to detect local conditions such as no edge, weak edges or ramp

edges and sharp edges, respectively. The choice of these thresholds may be determined from statistical analysis or by examining the generalized gradient image histogram. These thresholds give the processor a flexible choice for different image types and different processing purposes [see Fig. 3].

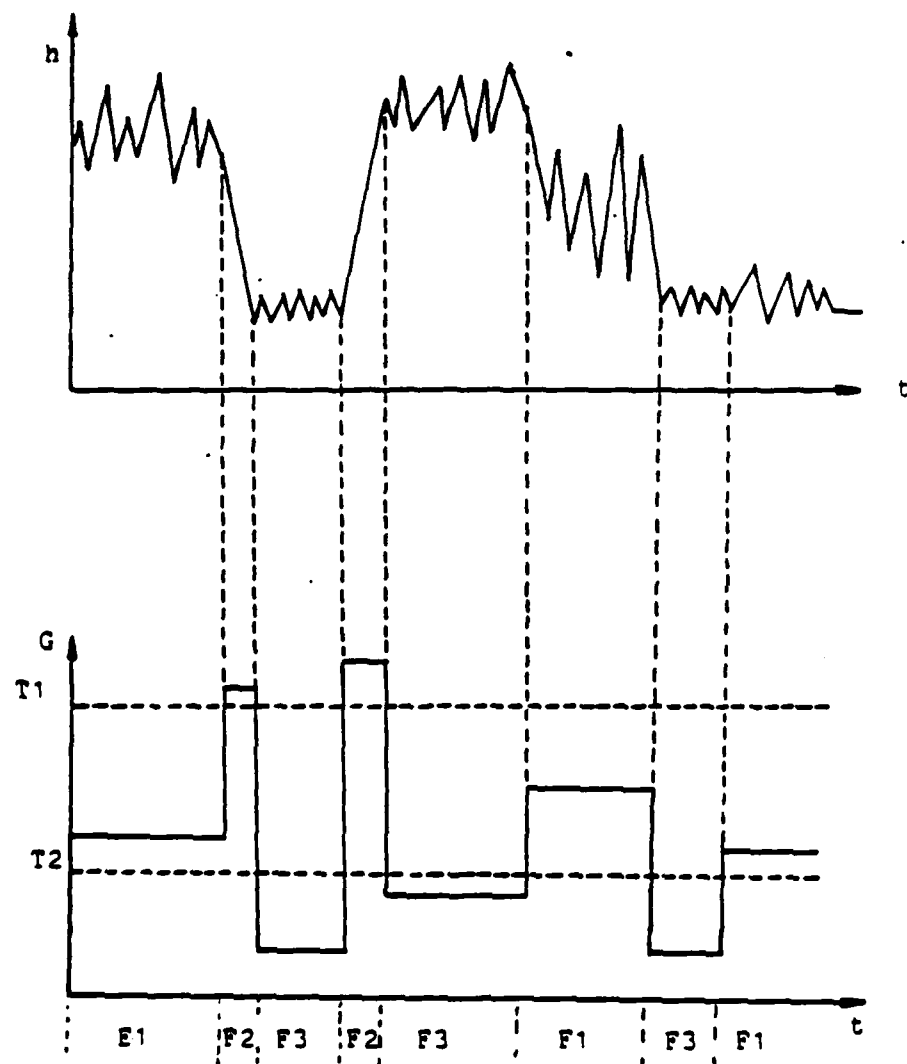


Figure 2. Principle of MTA filter: T1-threshold 1,
T2-threshold 2, F1-Sigma filter F2-Medain
filter, F3-Averaging filter.

A thresholding operation is used to determine a set of zero-one weights according to the value of G_{ij} such that the filtering will be adapted to different strategies F_m , $m=1, 2, \dots, k$ which are the different replacement rules for the central pixel in the $N \times N$ window.

Strategy F_m is chosen if

$$T_{m-1} < G_{ij} < T_m .$$

In our experiments, the set of weights are chosen such that the filtered pixel value w_{ij} is given by

$$w_{ij} = \begin{cases} A_{ij} & \text{if } G_{ij} < T_1 \\ S_{ij} & \text{if } T_1 < G_{ij} < T_2 \\ E_{ij} & \text{if } (G_{ij} > T_3) \text{ AND } (\max_{N \times s} G^{Ns/4} = G^0_s) \\ & \text{OR if } (T_2 < G_{ij} < T_3) \\ M_{ij} & \text{if } (G_{ij} > T_3) \text{ AND } (\max_{N \times s} G^{Ns/4} \neq G^0_s) \end{cases} \quad (4.7)$$

where A_{ij} is the output of a 5 by 5 averaging filter and S_{ij} is the output of a 7 by 7 sigma filter[4] and E_{ij} is the output of the eight edge direction weighted filter[5] and M_{ij} is the output of a 3 by 3 Median filter[6].

As a result, the averaging filter is only applied to very homogenous regions; this avoids bluring the weak texture. The median filter is only applied to those regions which have sharp edges; this avoids eliminating the lines, small objects

and avoids creating artifacts in other regions. The sigma filter is only applied to those regions where the weak texture preserving is more important than perfect noise cleaning. Thus, a balanced texture preserving and noise removal effect can be simultaneously achieved.

IV STATISTICAL LABELING AND ADAPTIVE RELAXATION

In this chapter we describe a statistical labeling algorithm to discriminate the shadow regions from the water regions on radar imagery in the pixel level.

At the low level, we first have to extract the statistical parameters. It is well known that texture is an important feature to characterize and discriminate regions. The two major texture analysis approaches are the statistical and structural ones. Since the texture on the radar image does not contain any very regular "texture units" and their spatial arrangements are random, the statistical approach to extract these natural texture features would be the most appropriate way.

A variety of texture analysis methods have been developed. They can be found in [12 ,13]. One of the most widely used method is the gray-tone co-occurrence matrices (GTCM) proposed by Haralick et al. [7]. Because human beings are sensitive to second-order statistics [14] and the GTCM method is based on the estimation of such second-order statistics, it is reported that the GTCM method is more powerful than the other methods [15]. The GTCM method can be briefly summarized as follows:

Let $f(x,y)$ be a rectangular digital picture and let N be the number of gray levels in f . The GTCM is a square matrix

M of dimension $N \times N$. The (i, j) th entry in M , denoted by M_{ij} , is a function of the image gray tone values and a displacement vector $d = (d_1, d_2)$. The entries M_{ij} are the unnormalized counts of how many times two neighboring resolution cells which are spatially separated by d occur on the image, one with gray tone i and the other with gray tone j . That is

$$M_{ij} = \# \{ ((m_1, n_1), (m_2, n_2)) \mid f(m_1, n_1) = i, \\ f(m_2, n_2) = j, ||(m_2, n_2) - (m_1, n_1)|| = d \} \quad (5.8)$$

where $\#$ denotes the number of elements in the set.

Haralick has proposed a variety of measures that can be used to extract useful texture information from the GTCM. Here, we choose two texture features. One is the entropy F_e , the other is inverse difference moment F_i . They are defined by

$$F_e = - \sum_i \sum_j M_{ij} \log(M_{ij}) \quad (5.9)$$

$$F_i = \sum_i \sum_j \frac{1}{1 + |i - j|} M_{ij} \quad (5.10)$$

The average entropy has a higher value than other texture features for an image with the same gray tone levels [7]. Since this measure is largest for equal M_{ij} and smallest when they are unequal, the entropy measure is useful to enhance

bright linear features and weak texture values. The usefulness of the inverse difference moment texture feature for classifying radar image segments was demonstrated by Shanmugan et al [8]. The histogram of these two texture features in a sampling area show that they exhibit a Gaussian distribution shape. In one-dimensional feature space, however, the distributions of the samples of water and shadow clearly overlap. This indicates that a single parameter may not sufficiently characterize the texture. Therefore, we use the gray tone value, the entropy value and the inverse difference moment value as three measurements to form a three dimensional measurement vector X .

By examining the histogram of the sample of the above three measurements, these data appear to have a Gaussian distribution. Thus, the Gaussian Maximum Likelihood decision rule can be used for the initial labeling process. It assigns measurement vector X to class ω_r , if and only if

$$P(X | \omega_r) P(\omega_r) = \max_p P(X | \omega_p) P(\omega_p) \quad (5.11)$$

where

$$P(X | \omega_r) = \frac{1}{(2\pi)^{N/2} |\Sigma|^{1/2}} \exp\left(-\frac{1}{2} (X - \mu_r)^T \Sigma_r^{-1} (X - \mu_r)\right)$$

is the class-conditional density function,

$\mu_r = E [X | \omega_r]$ is the class conditional mean vector which is estimated from training samples for class ω_r .

$$\Sigma_r = E [(X - \mu_r) (X - \mu_r)^T]$$

is the class conditional covariance matrix which is estimated from training samples for class ω_r , and

$P(\omega_r)$ = prior probability for class ω_r . If this is unknown, we can assume that all prior probabilities are equal.

In order to improve the labeling performance, a contextual classifier using a non-degradation adaptive relaxation algorithm can be applied to the radar image. Probabilistic relaxation labeling algorithms, which reduce ambiguity and noise and select the best label among several possible choices, have been an attractive practice in many types of image data processing [16-18 and 10].

However, unlike simple object labeling such as in the tetrahedral block world where there exists a small number of legal labelings, pixel labeling in radar image data classification has enormous ambiguity and the contextual information is generally not known. Furthermore, in pixel labeling the probabilistic relaxation procedure generally shows a degradation after several iterations. In some situations the results after many iterations can be worse than the initial labeling. Since the number of iterations for minimum error

is unknown in advance, there is a potential problem for the use of probabilistic relaxation [19]. This is an especially serious problem in the case that the ground truth data are difficult or impossible to get.

There are two ways to solve this problem. One is to try to extract most of the context in the data in the first few iterations so that the initial labeling information is used in a sufficient and correct manner. The other is to try to take the local pixel label dependencies into the relaxation labeling process, so that the process from one region into another cannot get out of hand. Kalayeh and Landgrebe [20] suggested one adaptive labeling method using the weighted sum neighbor function to attempt to solve this problem. Instead of that, we describe a method for our system using a non-weighted product neighbor function in which the compatibility coefficients are dynamic. Consequently, it results in a fast convergence speed and a better accuracy in the relaxation process. We initially classify the pixels probabilistically on the basis of certain specific features and then iteratively adjust the class probabilities based on its neighboring probabilities and the compatibility of the context. The procedures are as follows.

First, we compute the initial probabilistic labeling which is given by the normalized likelihood

$$P(q_i | d_k : \text{KGZ}_i(1)) = P(w_r | X)$$

$$= \frac{P(X | w_r) P(w_r)}{\sum_{w_p} P(X | w_p) P(w_p)} . \quad (5.12)$$

In the above formula, we use the notation $P(q_i | d_k : k \in Z_i(1))$ to denote the initial labeling probability which is the probability that unit i takes the label q_i given the first level context, where q_i corresponding to class w_r can be each class from the set $\Omega = \{w_1, w_2, \dots, w_m\}$, and d_k is the measurement made of unit i and $Z_i = \{1\}$ indicates that pixel i is the entry unit in the first level context for unit i [9]. The relaxation begins with $P(q_i | d_k : k \in Z_i(1))$. For the sake of simplifying notation, we will denote it by $P(q_i, 1)$.

From a Bayesian point of view, let us consider the probabilistic relaxation algorithm [9]

$$P(q_i, t + 1) = \frac{P(q_i, t) Q(q_i, t)}{\sum_{q_i} P(q_i, t) Q(q_i, t)} . \quad (5.13)$$

where $P(q_i, t)$ is the conditional probability that unit i takes label q_i given the t^{th} level context, and $Q(q_i, t)$ is the t^{th} estimate of the neighborhood function which indicates the degree of neighbor support for that conditional probability.

There are different possible combinations for the support $Q(q_i, t)$ which the neighbors give the current unit. Typically we have

- 1) the weighted sum of their supports

$$Q(q_i, t) = \sum_{j \in N(i)} D_j \sum_{q_j} P(q_j | d_k : k \in Z_j(t)) J_{ij}(q_i | q_j) . \quad (5.14)$$

- 2) or the product of their supports

$$Q(q_i, t) = \prod_{j \in N(i)} \sum_{q_j} P(q_j | d_k : k \in Z_j(t)) J_{ij}(q_i | q_j) . \quad (5.15)$$

where $N(i)$ is the set of neighbors for unit i , and D_j is the total influence that a particular neighbor j can have on unit i , and d_i is the measurement made of unit i , $Z_i(t)$ is the set of units in the t^{th} level context for unit i , and $J_{ij}(q_i | q_j)$ are the compatibility coefficients which represent the compatibility between the unit i with the label q_i and its neighbor with the label q_j .

The compatibility coefficient $J_{ij}(q_i | q_j)$ is the key term that decides the extent of support in neighbor function $Q(q_i, t)$. In the relaxation process, the context at each iteration grows by an entire neighborhood width surrounding the previous level context. The initial measurement made of unit i is its immediate context. The neighborhood context for unit i is the measurement d_i plus all the measurements of units in the neighborhood of unit i . The next larger context for

unit i is the measurement d_i plus all the measurements of units in the neighborhood of unit i plus all the measurements of units in the neighborhood of the neighbors of unit i .

Based on above theory, we have two considerations for determining the compatibility coefficients $J_{ij}(q_i|q_j)$. One is that the contextual information should be extracted only in the fewest number of iterations, so $J_{ij}(q_i|q_j)$ should be based on the largest reasonable context for unit i . The other is that we should insure no degradation in whole process, so the compatibility coefficients should be variable and data dependent rather than a constant over the whole data set.

The problem is that the neighboring patterns of every pixel actually are unknown to us. The initial probabilistic labeling process only provides an estimate of the identities of neighboring unknown patterns. This estimate which is based on the feature measurements also has some uncertainties. This is why the initial labeling result has a number of errors and ambiguity. If we compute the compatibility coefficients just using the single pixel estimate in the nearest neighbor system, the initial labeling error will be incorporated into the compatibility coefficients. This will cause degradation in relaxation process. One way to solve this problem is to use a local average estimate instead of a single pixel estimate so that we can reduce the risk of using the incorrect contextual information. In order to do so, we make two assumptions. First, we assume that the majority of the initial

estimates in a chosen window are correct. Second, we assume that there exist some correlations between the neighbors. These assumptions are true in most cases.

Therefore we compute the adaptive compatibility function $J_{ij}(q_i|q_j)$ in the following way. By Bayes formula

$$J_{ij}(q_i|q_j) = \frac{P(q_i, q_j)}{P(q_j)} .$$

$$= \frac{P(q_i) P(q_j|q_i)}{P(q_j)} . \quad (5.16)$$

Using the local average estimate, we choose:

$$P(q_j) = \frac{1}{|N(j)|} \sum_{a \in N(j)} P(q_a | d_k : k \in Z_a(1)) \quad (5.17)$$

where $j \in N_1(i)$ and $N_1(i)$ is the nearest neighbors of unit i , and $N(j)$ is the set of neighbors surrounding the neighbor set $N_1(i)$ for unit i .

For the same reason we choose

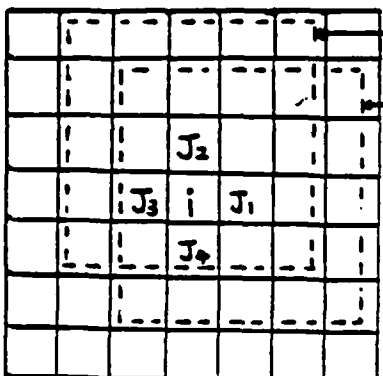
$$P(q_i) = \frac{1}{|N_2(i)|} \sum_{b \in N_2(i)} P(q_b | d_k : k \in Z_b(1)) \quad (5.18)$$

where $N_2(i)$ is a set of neighbors of unit i , however, $N_2(i)$ is the second order neighbor set and $N_1(i)$ is the nearest neighbor set. Since we have expanded the unit i to all its neighbors b in order to estimate $P(q_i)$, so should we also consider all b 's neighbors $N(b)$ when we estimate $P(q_j|q_i)$. By approximating the conditional probability we choose

$$P(q_j|q_i) = \frac{1}{|N(b)|} \sum_{c \in N(b)} P(q_c | d_k : k \in Z_c(1)) \quad (5.19)$$

where $N(b)$ is a set of neighbors of neighbor $N_2(i)$ for unit i .

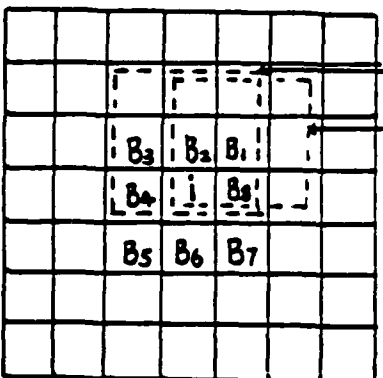
The relationship between these neighbor sets are shown in Figure 3.



N (J_2)

N (J_1)

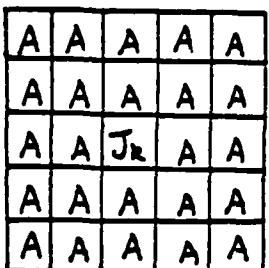
1. THE 7×7 WINDOW AND THE NEAREST NEIGHBORS $N_1(i)$. i IS THE PIXEL TO BE UPDATED AND $i = J_5$.



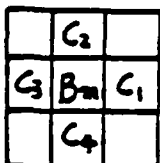
N (B_2)

N (B_1)

2. THE SECOND ORDER NEIGHBORS $N_2(i)$. i IS THE PIXEL TO BE UPDATED AND $i = B_9$.



3. THE NEIGHBORS $N(J_k)$ OF THE NEIGHBOR $N_1(i)$ FOR ESTIMATE J_k , WHERE $k=1,2,3,4,5$.



4. THE NEIGHBORS $N(B_m)$ OF THE NEIGHBORS $N_2(i)$ AND $m=1,2,\dots,9$

Figure 3. Relationship of the neighbor sets.

The weighted sum neighbor function which Kalayeh and Landgrebe use does not reach the optimum result. Because in adaptive relaxation, we already use the local average, it is unnecessary to set the weights to adjust compatibility again. Furthermore, the situations in remote sensing data are complicated. There is no guarantee that setting the weights can achieve all desired effects simultaneously. In fact, we can not take care of the variety of different cases by using a single set of weights in the whole updating process. Thus, the weights may introduce a bias effect in this adaptive relaxation. As an attempt to improve it, we use the non-weighted product neighbor function in which the compatibility coefficients are adaptive and dynamic. That is

$$\Omega(q_i, t) = \prod_{j \in N(i)} P(q_j | d_k : k \in Z_j(t)) J_{ij}(t). \quad (5.20)$$

where $J_{ij}(t)$ is the compatibility coefficient $J_{ij}(q_i | q_j)$ after t iterations. It is computed according to the updated q_i and q_j . Because there is no degradation in adaptive relaxation, after the end of the iterations, we obtain more context information. Then we can compute the new compatibility coefficients which reflect the new accurate relationship between the pixels to be updated further and its neighbors. Thus, the compatibility coefficients are further adapted to a new level. This technique speeds up the convergence process. In

order to compare our method with that of Kalayeh and Landgrebe, we run both methods on the same data and find that our method has a better accuracy in fewer iterations.

Using the above technique, we compute the compatibility coefficients $J_{ij}(t)$ for every pixel in the remote sensing data. The immediate context, the neighborhood context and the next larger context are measured once and combined into $J_{ij}(t)$. As a result, $J_{ij}(t)$ slowly varies from pixel to pixel and from iteration to iteration. Then a non-weighted product neighbor function $Q(q_i, t)$ is computed. Finally, we assign the pixel to that class which has the highest probability after relaxation.

V USING A RELATIONAL MODEL TO REDUCE AMBIGUITIES

Relational models are commonly used in scene analysis system. One important use of relational models in scene analysis is to help identify an unknown object that has been extracted from a scene. A structural description of an unknown object can be constructed and compared with known structural descriptions to determine how similar they are. The organization of relational models for scene analysis can be found in [21].

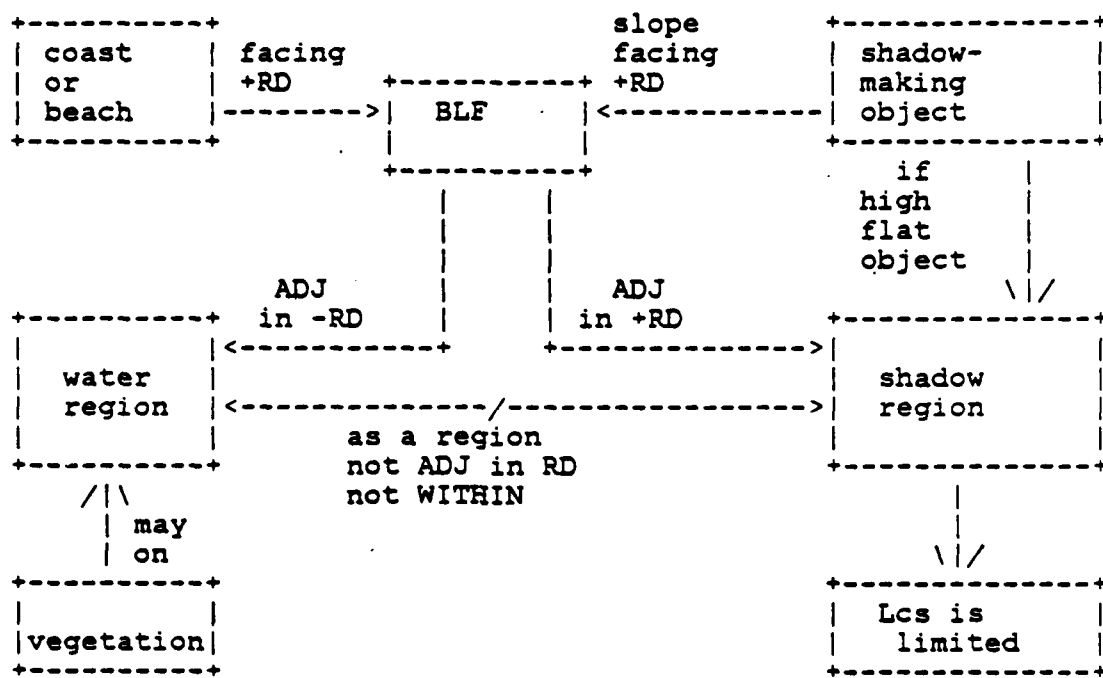
Since some objects in a scene, such as water regions and shadow regions in SAR image, are very difficult to distinguish between one another completely, and since the pictorial similarity is not always a reliable criterion for segmenting a scene into regions that completely correspond to the object classes, the low level labeling results provided by the statistical contextual classification may be incorrect. Obviously, only those labels that can be derived from an arrangement of real objects in the scene are valid. Properties of objects and relations between them imply corresponding properties and relations of the SAR image regions that result from these objects. These projected properties and relations contain the possible labelings of regions with object identification. So the goal that we try to achieve here

is to just use high level contextual information to verify the objects and reduce the ambiguities.

There is a way to use the context provided by the more easily recognized objects to determine other objects. More generally, we can use the spatial or contextual relationships between structural features or primitives provided by the statistical classification to match against the relational model based on our prior knowledge.

According to our analysis in Chapter II, a relational graph model for discriminating water and shadows can be generated [see Fig.4]. This model is represented by an abstract relational structure in which the nodes represent regions labeled with their property values and the arcs represent the relationships among regions. Usually, such model is often very difficult to formulate, since the constraints on allowable property values and relationships are hard to define. However, the results that we have from our low level classification provided better labeling accuracy than a simple segmentation did. Therefore the relational graph model that we need is much simpler than the usual one. From Chapter II, it is obvious that all shadow regions on the radar image result from three-dimensional objects on the terrain surface. These objects are called shadow-making objects, and the corresponding regions are called shadow-making regions. Note that a shadow-making object is not necessarily an object which is in shadow on the image. However, it causes an adja-

cent object to be in shadow. We extract the shadow and shadow-making region pair in two steps. First, we extract the regions which are adjacent in radar look direction to dark regions. Second, we select the regions which have a long common boundary with a neighboring dark region in the direction away from the radar antenna. If the adjacent shadow-making objects are not flat, then the extraction of shadow-making regions becomes simply the extraction of bright linear features.



where +RD: radar look direction.

-RD: opposite to +RD.

Lcs: length of shadow region along +RD.

BLF: bright linear features.

---->: spatial relation.

ADJ: adjacent.

Figure 4. Relational graph model: for water, shadow and others.

According to the relational model, a set of decision rules are determined as follows:

Assign a region to shadow, if the region is in either of the following two cases:

- 1) A region which is assigned to shadow by the low level labeling is surrounded by other non-water regions.
- 2) A region which is assigned to shadow by the low level labeling is adjacent to bright linear features in the radar look direction.

Assign a region to water, if it is in one of the following cases:

- 1) A region is assigned to water by the low level labeling is adjacent to bright linear features in the radar look direction.
- 2) A region which is assigned to water by the low level labeling is surrounded by other non-shadow regions.
- 3) A region which is assigned to water by the low level labeling has a length longer than the specified limitation of shadow length along the radar look direction.
- 4) A region which is assigned to water by the low level labeling has some vegetation on it.

Assign a region to be a false shadow region and merge it to its surround, if the region is in one of the following three cases:

- 1) A region which is assigned to shadow by the low level labeling is surrounded by a water region.

2) A region which is assigned to shadow by the low level labeling has a length longer than the specified limitation of shadow length along the radar look direction.

3) A region which is assigned to shadow by the low level labeling is between a water region and some other non-shadow region.

Assign a region to be a false water region and merge it to its surround, if the region which is assigned to a water region by the low level labeling is surrounded by a shadow region.

For the above relational model, the shapes of water regions and shadow regions are arbitrary, so the classical region attributes to represent an object such as medial axis etc. are not helpful in this situation. Also, the representation of regions by circumscribing boxes is not suitable for our case, because sometimes a spurious adjacent or surround relation will hold between boxes of two regions, while in fact it is not true of the regions themselves. We choose several structural measurements for the regions. They are: the size of the region; the relative position of different adjacent regions along the radar look direction; the maximum length of the region along radar look direction, the region state (interior to the image or touching the boundary of the image) and the number of its boundary pixels. The algorithm for measuring these spatial relations is as follows.

First, the region indexes of the symbolic image obtained from low-level processing are redefined. Each region is identified by a unique region identifier. However, in the three digit index, the first digit represents the original low level labeling. For example, the water region index starts from 100 and the shadow region index starts from 200 etc.. Thus, we still can recognize the initial assigned label from the new sequential index.

Second, it uses a linear geometric transformation to rotate the symbolic image to a position such that the horizontal scanning line is parallel to the radar look direction.

Third, it scans the symbolic image line by line in the radar look direction. If the scanning line meets a new region label, the scanning process will be interrupted and a tracing process which traces the region's external boundary will start. We describe a one-pass, depth first boundary tracing procedure using a left first, clockwise directed four connected neighborhood search technique for tracing a region boundary:

- 1) Record the coordinates of the starting point of the region, keeping the region always on the right side of the tracing direction and trace the boundary in a clockwise direction.
- 2) For each successor, detect the next tracing direction by searching the same label from the four connected neighbors in the order starting from the left side of previous moving

direction, then the front, the right, and finally the back [Figure 5],

3) Record the left side adjacent region label and its starting position and end position in the tracing process.

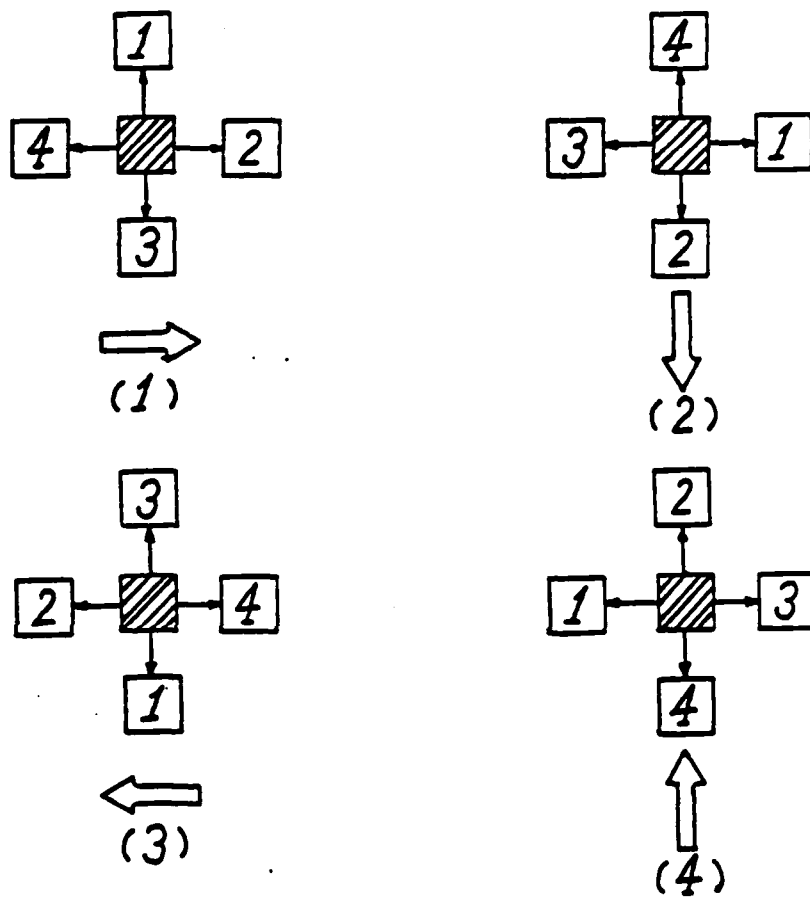
4) Count the number of pixels of the region boundary in the tracing process.

5) Mark the region state. Mark 0 indicates that the region is completely within the image. Mark 1 indicates the region touches the image boundary.

6) If next point=starting point, then stop tracing, go to step 7, else go to step 2.

7) Continue the scanning process from the break point. Compute the maximum region length along radar look direction and the region size,

8) Check every label that the scanning line met with by means of a hash table. If the region has been traced, go to step 7, else go to step 1, until the last line.



➤ Previous moving direction.
 ■ Current position
 □ Neighbors to search

Figure 5. Direction and order of searching: previous moving direction (1) left to right, (2) top to bottom, (3) bottom to top, (4) right to left.

The high level image analysis techniques require rapid access to region information and to the relations between regions. For every region, therefore, the region attributes and the relations of adjacent regions (between or surround) are stored in a big list. And a hash function is used for fast searching and accessing to this structural information. After that, a property file which contains a list of property values for the above measurements can be created. Then the spatial reasoning process simply becomes a table-look up procedure according to the structural decision rule described previously.

To simplify the algorithm further, it is necessary to eliminate many small regions composed of a few pixels. This is reasonable, because our low level classification based on texture features is a local, not pointwise, phenomenon. It cannot be computed reliably for small regions or boundary cases. As a result, ambiguities may occur in a small size of object and the boundary region.

VI. EXPERIMENTAL RESULTS

A set of SAR images was tested using the system described in this paper. These images were collected over Huntsville, Alabama on 17 June, 1977 and collected over Elizabeth City area on 10 October, 1980. Because the initial data have a very wide gray tone range, we quantized the data into 64 or 128 gray tone levels for convenience of processing.

EXPERIMENT 1

In this experiment, a set of basic investigations are carried out on the radar image data. We examine the histograms of the radar images in the different cases. In the original image, the gray tone values spread from 0 to 65535, but most of them are within the interval between 1400 to 4000. After requantization, the histogram shows that the gray tone values are distributed from 0 to 63 with a mean 21.6 and variance 328. From both histograms, we see that their distribution shapes are like [see Figure 8 and Figure 9]. Comparing the histogram of the sampled water region with that of the sampled shadow region [Figure 10 and Figure 11], we can see that the gray tone values in both regions are very low and they clearly overlap from 0 to 16. However, the mean and variance of the sampled water region are lower than those of the sampled shadow region. By examining the histogram of

texture entropy values [Figure 12], we see that it has a bimodal shape distribution. The left mode may be the values of possible water and shadow regions and the right mode may be that of others. To see the difference of entropy value in water region and shadow region, we examined the entropy values in both regions [Figure 13, 14]. The result is that they overlap each other in an interval between 44 to 75. It is different from the gray tone histograms in that the entropy distribution of the shadow region shifted a little right to that of the water region. Meanwhile, the mean and variance of entropy of shadow region are also greater than that of water region.

Almost the same situation occurs in the histogram of inverse different moment texture values [Figure 15 to 17]. It is noted that the histogram of inverse different moment in the sampled shadow region is distributed widely from 44 to 186. This means that it overlaps with that of other land regions also. More comparisons were made by examining the histograms of texture values of the filtered SAR images [Figure 18 to Figure 23]. The results show that the differences of mean and variance of texture values between the water and shadow regions in the filtered image are greater than that of those regions in the image before filtering.

From above examinations, we conclude the following properties: 1) the requantized image almost keeps the same distribution shape with that of initial image; 2) the histogram

of the sampled water region clearly overlaps that of the sampled shadow region in any one-dimensional feature space (either the gray tone, entropy and inverse difference moment); 3) the histograms of three features in the filtered image are really different from the original image, although this effect can not be seen in the corresponding gray tone images; 4) most of histograms exhibit a Gaussian like shape.

All of these provide useful information for our recognition task. For example, point 2) indicates that a single parameter may not sufficiently discriminate the water region from the shadow region in a radar image. This is further confirmed by the following experiment in which the algorithm proposed by Davis et al[14] is used. We extract the interesting regions by 1), computing texture cooccurrence gray tone levels, 2), averaging the results, and 3), thresholding. The results show that this procedure can not discriminate the shadow from the water. These two categories are mixed [see Figure 24 to 27].

Also, the bright linear features present in the radar image are examined. We use the GTCM to segment the image into three categories. The first category consists of possible water or shadow regions. The second category consists of bright features. The third category is everything else. The GTCM preserves the bright lines and provides a structural feature for the relationship between these lines and the possible water or shadow regions [Fig.28 to Fig.30]

EXPERIMENT 2

To show the effects of using the Multi-Threshold Adaptive filtering, several SAR images were processed and compared. The corresponding generalized gradient image [Fig.32] shows the different local activities. The black color indicates the lowest local activity so that the moving average filtering was applied. The white indicates the highest local activity so that the Median filtering was applied. The blue and the red indicate cases between above two situations so that the Sigma filtering and weighted edge filtering were applied, respectively. Thus, different filtering strategies were applied to the regions according to the generalized gradient image. It seems that there is no obvious change between the original image [Fig.8] and the filtered image [Fig.31]. Almost every thin line, fine feature and basic texture in the image are preserved. However, there are significant changes that we can see from the textural image. It is clear that the entropy and the inverse difference moment computed from the filtered image are different from that of the original one [Fig.35 to Fig.38]. These changes are due to the removal of the noise. The interesting thing is that these changes can be controlled by setting different thresholds. Fig.34 shows the results from another set of threshold values. The generalized gradient image here is changed and it turns out

that more details and weak texture would be preserved in this case.

To see how the MTA filter improve the low-level labeling result more obviously, we added Gaussian normal noise $N(0, \sigma^2)$ with different σ values to the SAR images. Then the same statistical classifier as we described in Chapter IV were applied to the noisy image, the filtered image and the original image, respectively. The relative classification accuracy is measured by comparing them with that of original image classification [see Table 1 to Tabel 3]. It can be seen from these results [Figure 39 to 41] that the labeling accuracy of the image filtered by MTA filtering is much better than that of the noisy one. Before filtering, almost all the water regions in the noisy image were mislabeled as shadow regions and some shadow regions were mislabeled as others [see Figure 40]. However, for the filtered image, the labeling result was as good as the that of original one [see Figure 41]. The tables show that the relative accuracy can be improved from 61.9 percent to 92.2 percent (with noise $\sigma=10$), even from 65.5 percent to 96.5 percent (with noise $\sigma=5$).

Table 1. Contingency tables for classification results
 of noisy image and MAT filtered image
 (column = assigned class, row = true class,
 WR = water, SD = shadow, OT = others).
 Scale factor for the number of pixels = 100.
 Noise $\sigma=10$ for the noisy image.

Table 1 (a) Result for noisy image

class	WR	SD	OT	total	Acc(%)
WR	7	0	1	8	0.7
SD	857	121	57	1035	73.3
OT	41	44	1494	1579	96.3
total	905	165	1552	2622	61.9 * & b.

Table 1 (b) Result of MTA filtered image

class	WR	SD	OT	total	Acc(%)
WR	831	25	1	857	91.8
SD	63	130	95	288	78.7
OT	11	10	1456	1477	93.8
total	905	165	1552	2622	92.2 *

* overall classification accuracy: ratio of the number
 correctly classified pixels to the number of total
 classified pixels.

Table 2. Contingency tables for classification results
 of noisy image and MTA filtered image
 (column = assigned class, row = true class,
 WR = water, SD = shadow, OT = others).
 Scale factor for the number of pixels = 100.
 Noise $\sigma=5$ for noisy image.
 *: Overall classification accuracy.

Table 2 (a) Result of noisy image

class	WR	SD	OT	total	Acc(%)
WR	64	0	2	66	7.1
SD	827	142	40	1009	86.1
OT	13	23	1511	1547	97.3
total	904	165	1553	2622	65.5*

Table 2 (b) Result of MTA filtered image

class	WR	SD	OT	total	Acc(%)
WR	875	19	1	895	96.7
SD	27	132	30	189	80.0
OT	3	14	1521	1538	99.9
total	905	165	1522	2622	96.4*

Table 3. Contingency tables for classification result
of noisy image and MTA filtered image
(column = assigned class, row = true class,
WR = water, SD = shadow, OT = others).
scale factor for number of pixels = 100.
*: Overall classification accuracy.
Noise $\sigma = 3$ for noisy image.

Table 3 (a) Result of noisy image

class	WR	SD	OT	total	Acc (%)
WR	681	2	3	686	75.2
SD	220	146	32	398	88.5
OT	4	17	1517	1538	99.7
total	905	165	1552	2622	89.4

Table 3 (b) Result of MTA filtered image

class	WR	SD	OT	total	Acc (%)
WR	890	17	2	909	98.5
SD	13	133	22	168	60.6
OT	1	15	1528	1544	98.5
total	904	165	1552	2621	97.4

EXPERIMENT 3

The low level statistical labeling algorithm is examined in this experiment. Two radar images which definitely contain water regions and shadow regions are chosen as the test data. In the first image [Fig.6], the shadows are created by high reliefs (some of them are the intermediate case described in Chapter II). In the second image [Fig.48], the shadows are made by the high flat objects. The Gaussian Maximum Likelihood Classifier is applied to these two images. The feature space for classification consists of gray tone value and texture values. Then the 3-dimensional mean vector and 3 by 3 covariance matrix are estimated from the training sample set [Fig.42 and Fig.52] for the water region and the shadow region and others, respectively.

The texture features, both entropy and inverse difference moment, are extracted from the GTCM which are computed for different window sizes and different distances. The experiments show that the window size and the distance of GTCM have significant influence on the accuracy of classification. An unsuitable window size and distance may cause an incorrect texture feature extraction. As a result, ambiguities on boundary and mislabeling of the small regions will occur in the result.

It can be seen in classified images that there are some land regions which contain the water regions [Fig.43 and Fig.55]. This is a low probability event and probably represents a classification error. Also there are some shadow regions along the boundary of the water body [Fig.43]. This probably represents a classification error too. For the first image, the GTCM with a window size 12 by 12 and a distance 6 [Fig.46] produces the better result. For the second image, the classified image using a window size of 16 by 16 and a distance 8 has less ambiguities [Fig.57].

To improve the overall classification accuracy, the adaptive relaxation using contextual imformation is applied to the images of Figure 6 and Figure 48. The initial statistical labeling is determined by the normalized maximum likelihood estimate. The immediate context, the neighborhood context and the next larger context in the initial labeling are measured once and combined into the compatibility function. Comparing Fig.43 with Fig.44, Fig.57 with Fig.58 and Fig 59, the effect of reducing the ambiguity in the shadow regions is obvious. However, we can not expect this method to change the classified result too much, since the initial labeling error can influence the degree of the improvement. Further improvement can be obtained from the use of spatial relations between the structural features. By human interpretation, however, we can confirm that most classified regions, either water or shadow, in Fig.44 and Fig.59 are

correct. In other words, the low level classified results provide enough information for further structural recognition at high level.

To examine the performance of adaptive relaxation quantitatively, a set of LANDSAT MSS data collected from the Roanoke area in 1979 were tested. The initial labeling probabilities for 3 classes of urban or built-up land, agriculture and forest were estimated by the normalized maximum likelihood method. The initial non-context labeling results [Figure 61] were obtained by using Maximum Likelihood Decision rule. The black region is urban or built-up land, the white region is the agricultural land, and gray region is forest land. The corresponding mean and covariance matrix are shown in table 4. As ground truth in this experiment, we use the results of a hand segmentation obtained on basis of the spectral information from the corresponding aerial photographs [Figure 62]. The adaptive relaxation algorithm with dynamic compatibility coefficients $J_{ij}(t)$ were applied to a block of 150 x 150 pixels. The initial error of this block is 32.8 percent. Within three iterations, this error reduced to 25.2 percent. This experiment clearly shows that there is no degradation and most improvements of labeling accuracy are obtained in less than 5 iterations and then stabilized.

TABLE 4 The Mean and Covariance

Category 1 1116 pixels

Mean	Covariance Matrix			
23.507	8.1442	6.3528	1.7889	-0.93896
27.972		12.665	2.8140	-2.2597
43.950			18.394	20.999
41.680				31.051

Category 2 234 pixels

Mean	Covariance Matrix			
20.265	4.0409	5.6659	2.1560	0.19782
25.051		18.117	-0.05833	-7.2051
47.637			25.223	28.146
48.415				40.114

Category 3 533 pixels

Mean	Covariance Matrix			
15.448	7.2605	12.586	18.150	20.816
19.229		29.182	39.309	46.316
29.553			59.118	66.850
30.298				80.026

EXPERIMENT 4

To examine the performance of the structural recognition algorithm described in Chapter V, two symbolic images [Figure 44 and Figure 59] obtained from the low level labeling of SAR test image 1 and test image 4 were tested. After eliminating small regions and redefining the region index, the results are shown in Figure 65 and Figure 66. The radar look direction for both images is approximately from North to South (Top to Bottom), so we rotated the images 90 degrees before measuring their region attributes and relations. Using the depth first tracing strategy described in chapter V, the structural contextual features were measured and the corresponding property lists were created [see Table 5 and Table 6].

Table 5. The region attributes and relations list for
 Figure 65. (R1 = the surrounding region if R2=0.
 R2 = the second adjacent region that is not in
 the same class as R1.)

Region number	Region index	Max. length	Adjacent R1	Adjacent R2	State mark	Region size	Boundary length
1	100	416	201	0	1	7849499	3153
2	101	11	209	0	0	351	51
3	102	25	210	0	1	2592	88
4	103	65	233	0	1	85277	424
5	104	11	234	0	0	336	52
6	105	15	235	0	0	1113	67
7	200	20	300	0	1	3515	106
8	201	23	100	300	1	13587	1387
9	202	12	100	0	1	684	79
10	203	15	100	0	1	1928	115
11	204	36	302	100	1	46843	3663
12	205	16	300	0	0	1476	60
13	206	12	100	0	0	472	51
14	207	18	100	0	0	1156	94
15	208	9	302	0	0	459	55
16	209	32	302	0	0	12285	378
17	210	22	302	102	0	3629	297
18	211	11	100	0	0	494	41
19	212	14	302	0	0	742	63
20	213	9	100	0	0	344	37
21	214	20	302	0	0	3387	120
22	215	18	100	0	0	5184	370
23	216	13	100	0	0	1680	165
24	217	12	302	0	0	520	61
25	218	18	302	0	0	2378	125
26	219	16	302	0	0	848	84
27	220	17	302	0	0	1670	83

Table 5 The region attributes and relations list for Figure 65. (continued)

Region number	Region index	Max. length	Adjacent R1	Adjacent R2	State mark	Region size	boundary length
28	221	10	302	0	0	606	68
29	222	11	100	0	0	475	56
30	223	8	302	0	0	384	51
31	224	44	302	0	1	12302	291
32	225	20	100	0	0	1686	110
33	226	19	302	0	0	1501	105
34	227	12	302	0	0	476	53
35	228	13	100	0	0	1717	175
36	229	21	302	0	0	2013	100
37	230	24	302	0	1	2339	67
38	231	9	100	0	0	371	47
39	232	20	302	0	0	1293	92
40	233	29	302	103	1	5713	494
41	234	23	302	0	0	6147	194
42	235	20	302	0	0	3343	137
43	236	9	302	210	1	329	33
44	300	169	200	0	1	805522	968
45	301	13	201	0	1	736	61
46	302	512	204	0	1	12408839	3917
47	303	13	201	0	0	764	47
48	304	19	207	0	0	1911	60
49	305	27	215	0	0	5104	114
50	306	10	216	0	0	2368	133
51	307	47	215	0	0	15413	237
52	308	11	204	0	0	668	51
53	309	30	225	0	0	5590	80
54	310	10	228	0	0	2552	140

Table 6. The region attributes and relations list for
 Figure 66. (R1 = the surrounding region if R2=0.
 R2 = the second adjacent region that is not in
 the same class as R1.)

Reg. number	Reg. index	Max. length	Adjacent R1	Adjacent R2	State mark	Reg. size	Boundary length
1	100	319	300	204	1	9473378	2318
2	101	21	300	215	1	1156	105
3	200	21	300	100	0	6321	439
4	201	27	100	300	0	10056	543
5	202	18	300	0	0	1002	97
6	203	15	300	0	0	731	51
7	204	35	100	300	1	28028	927
8	205	24	300	0	0	2053	177
9	206	23	300	0	0	5229	229
10	207	14	300	0	0	902	100
11	208	24	300	0	0	12269	341
12	209	16	300	0	0	707	58
13	210	22	300	0	1	7097	376
14	211	34	300	0	0	24349	640
15	212	21	300	0	0	4591	203
16	213	31	300	0	0	27296	439
17	214	17	300	0	0	848	66
18	215	32	101	300	1	26779	406
19	216	22	300	0	0	3786	91
20	217	16	300		1	2184	83
21	300	448	200	100	1	16166526	2953

For image 1, there are 54 regions. According to the low level labeling, 6 regions were assigned as water regions, 37 regions were assigned as shadow regions and 11 regions are assigned as others. For image 2, there are 21 regions. In the low level labeling, two regions were assigned as water regions, 18 as shadows and one as others. From Table 5, we can see that there are several closed water regions (e.g. region 2, 5, 6) with small size are surrounded by shadows and some closed shadow regions (e.g. region 13, 14, 18, 20) are surrounded by water regions and some shadow regions (e.g. 11, 17, 40) with a longer maximum region length in radar look direction are between the water region and others. (A similar case can be found in region 7 and 18 in Table 6.)

By the structural decision rules described in Chapter V, which is based on the real world model described in chapter II, all these regions that we mentioned above are misclassified and should be corrected. Those regions with region state mark 1 are treated as partial regions. We are not sure whether they are surrounded by other regions or not. So we leave them alone. Finally, a new labeled image was generated according to the results of the spatial reasoning using the property lists. The results are shown in Figure 67 and Figure 68. Compared to the results of low level classification, the new results are more accurate. In a final experiment, the mean and covariance estimated from test image 4 [Figure 52] was used to classify another image [Figure 69] collected

in the same period and over the same area. The two texture features and the gray tone feature are used as before. Using the same statistical classifier, we got the low level labeling result which is shown in Figure 70. For the high level, the recognition results are shown in Figure 71 and Figure 72 and the corresponding property list is shown in Table 7. The results indicate that the high level recognition using the relational model can reduce the ambiguity so significantly that it allows the low level recognition procedure to be more flexible. It provides a way in which we may use a limited number of training samples in one image to recognize objects in a set of radar images collected in the same condition.

Table 7. The region attributes and relation list
 for figure 71. (R1 = the surrounding region
 if R2=0. R2= the second adjacent region that
 is not in the same class as R1.)

Region number	Region index	Max. length	Adjacent R1	state R2	mark	Region size	Boundary length
1	100	66	200	0	1	29282	241
2	101	21	303	203	1	1652	100
3	102	306	201	0	1	3938268	2095
4	103	21	300	227	1	1916	167
5	200	24	300	100	1	7359	221
6	201	75	300	102	1	201797	5866
7	202	32	303	0	1	11302	291
8	203	21	303	101	1	3089	181
9	204	18	302	0	0	1572	115
10	205	19	300	0	0	1157	132
11	206	25	303	0	0	3408	239
12	207	16	303	0	0	2429	175
13	208	22	300	0	1	5803	377
14	209	16	300	0	0	1536	214
15	210	18	303	0	0	2495	180
16	211	25	303	0	0	4546	142
17	212	26	300	0	0	2637	165
18	213	26	300	0	1	8456	287
19	214	25	300	0	0	15246	298
20	215	17	303	0	0	1593	73
21	216	25	303	0	0	3293	139
22	217	28	303	0	0	15058	186
23	218	25	303	0	0	5555	183
24	219	19	303	0	0	2813	232
25	220	27	303	0	1	4162	137
26	221	28	300	0	1	12511	171
27	222	15	303	0	0	3672	176
28	223	34	303	0	1	9155	185
29	224	29	303	0	0	14118	224
30	225	26	300	0	0	3526	110
31	226	19	303	0	0	3522	175
32	227	12	103	300	0	2323	266
33	300	373	200	103	0	6148748	3331
34	301	13	201	0	1	992	102
35	302	34	201	0	1	17413	215
36	303	36	201	101	1	9679777	3863

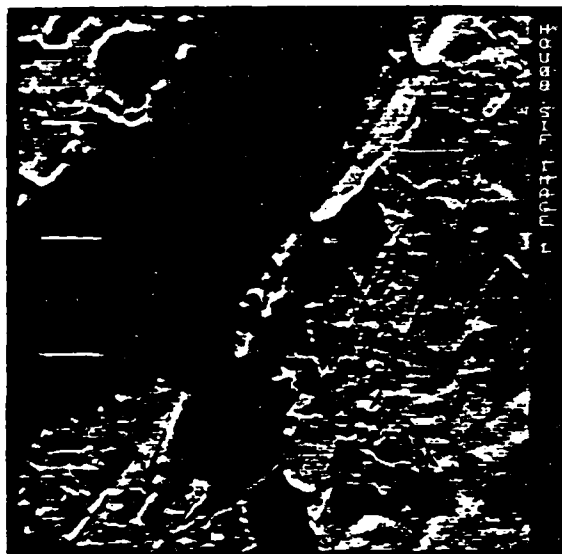


Figure 6. Test image 1: The large black region is water and the several small black regions separated in the land are shadow regions.

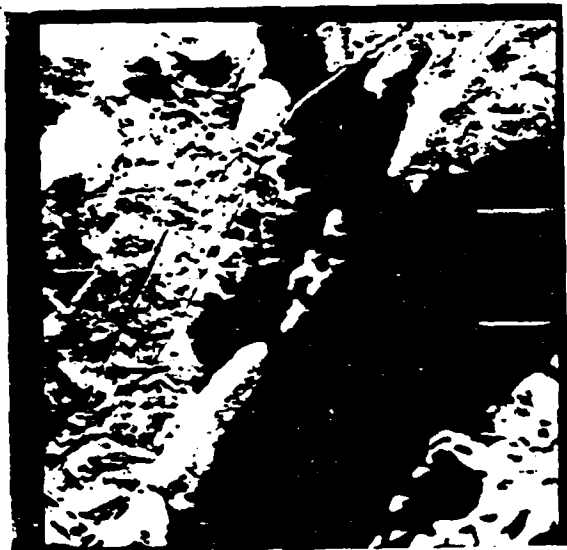


Figure 7. 64 level quantization of image 1

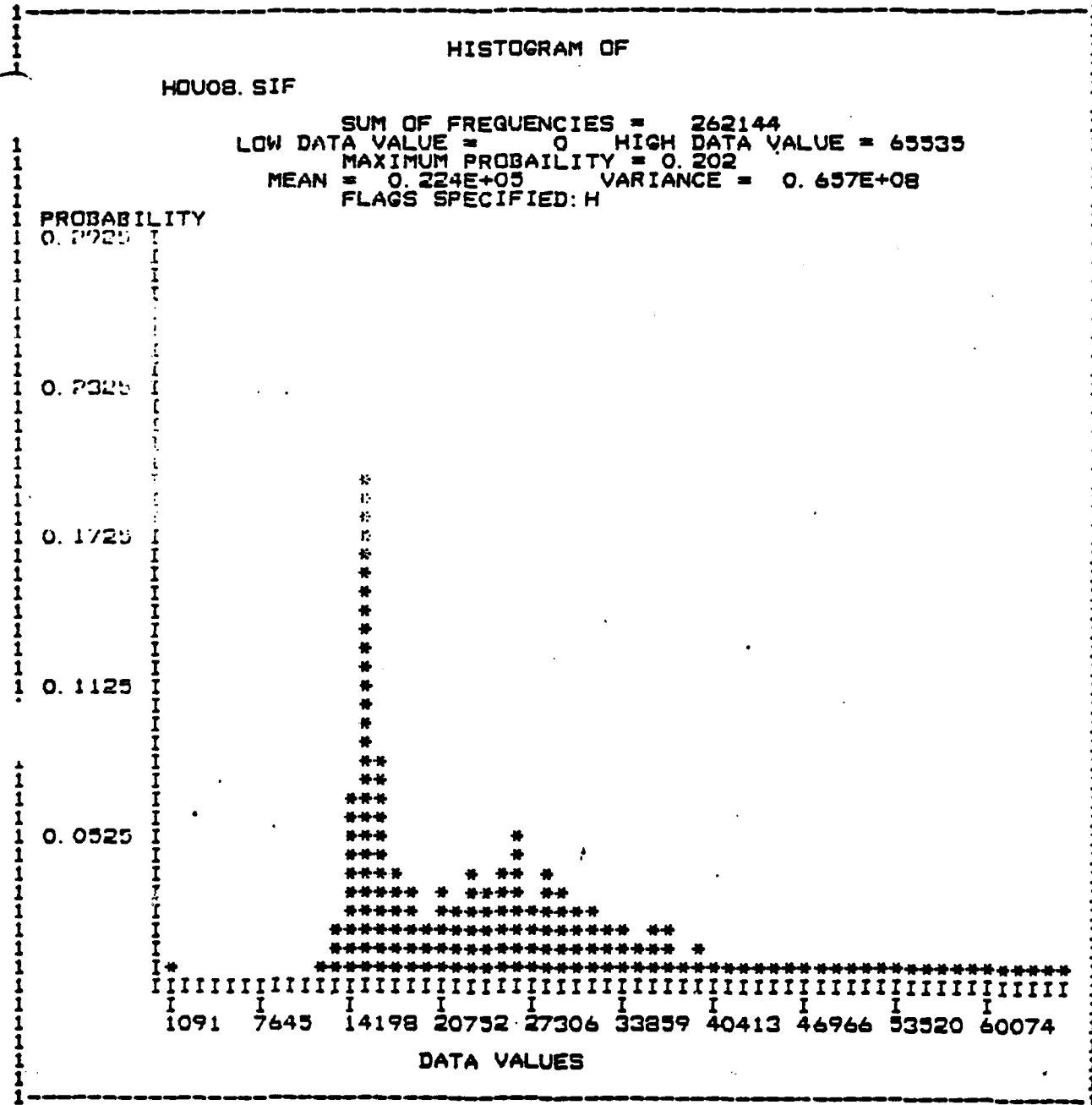


Figure 8. Histogram of image 1

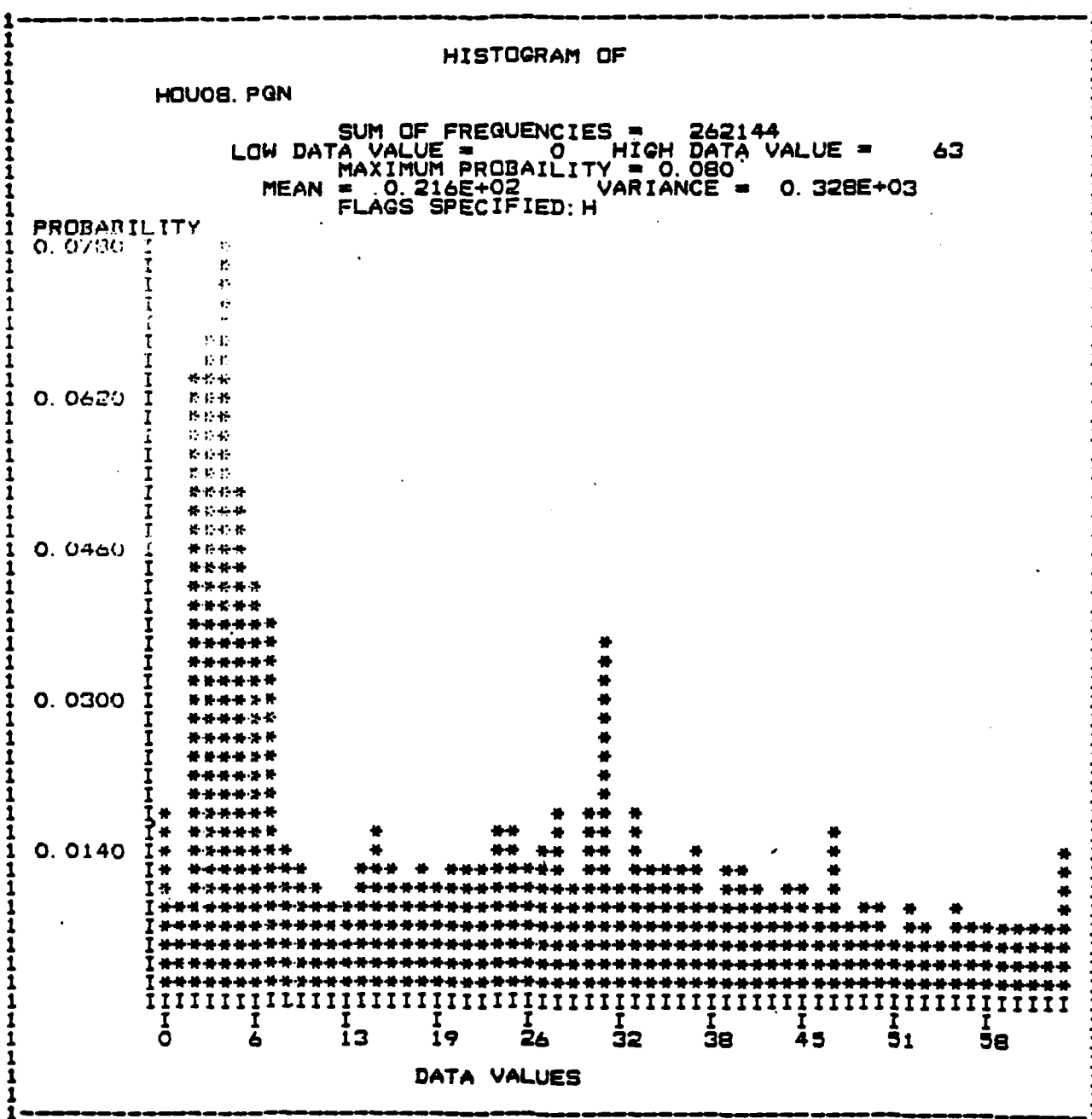


Figure 9. Histogram of quantized image 1:
 quantization level = 64.

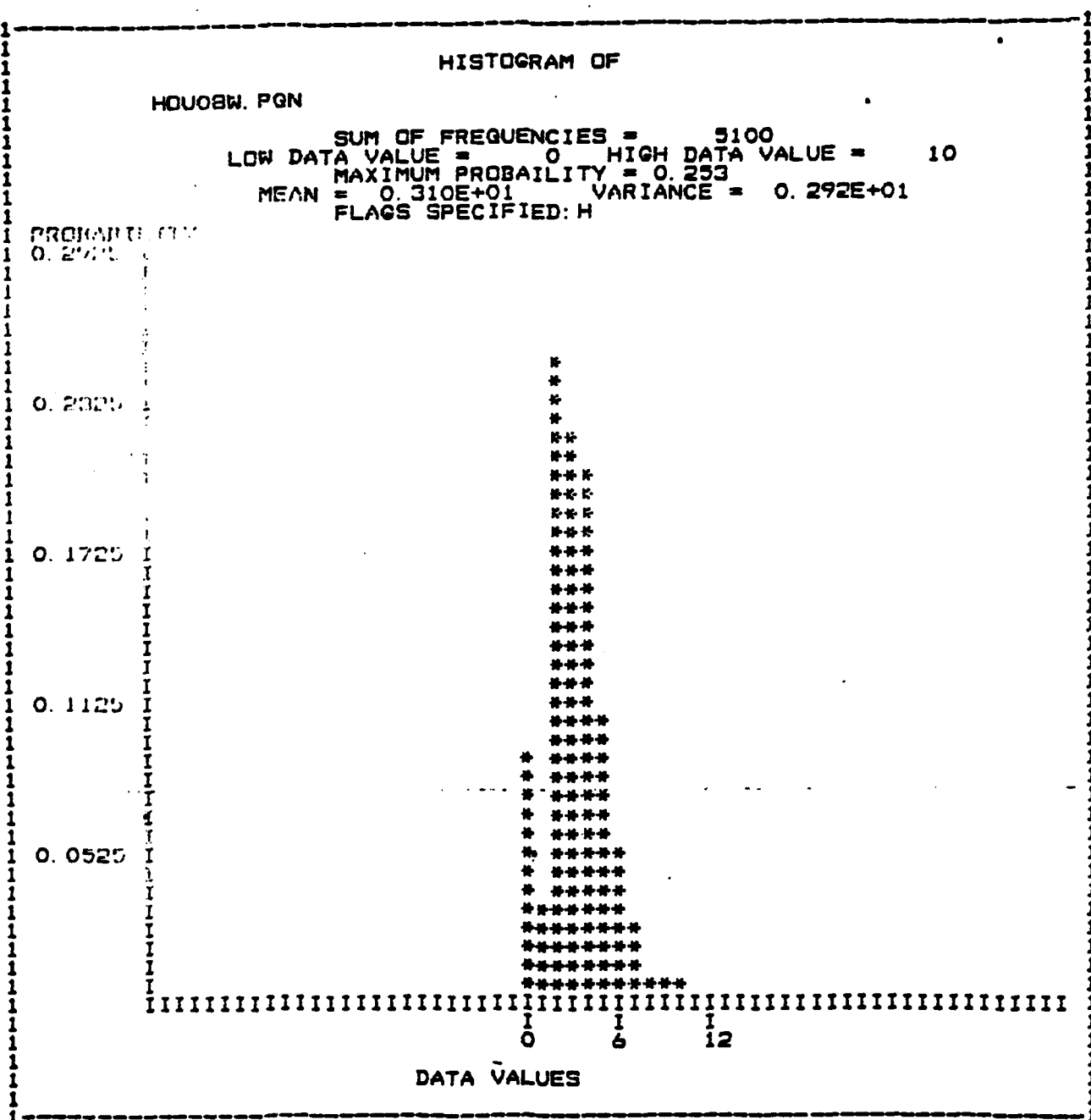


Figure 10. Histogram of sampled water area: from quantized image 1.

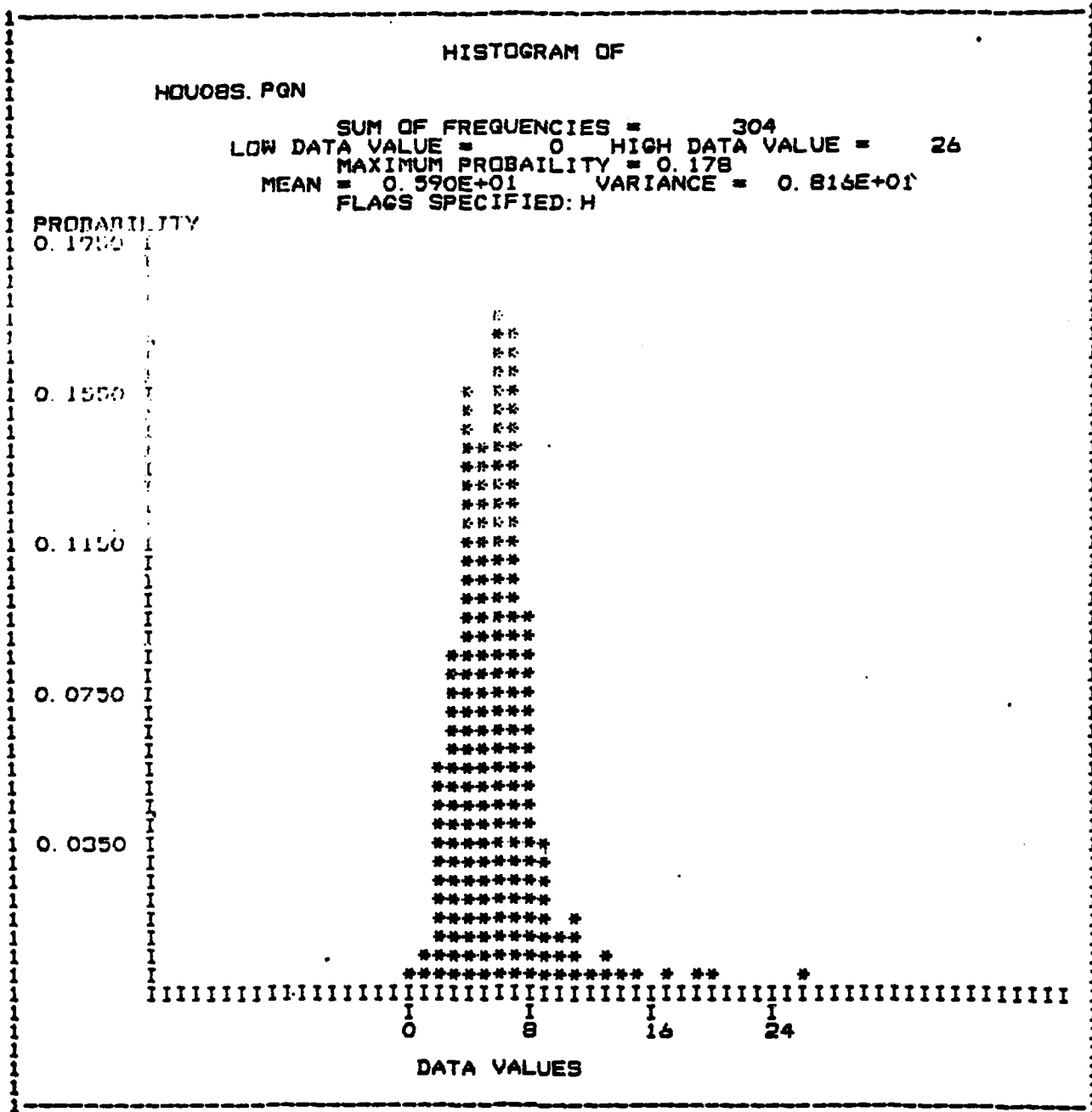


Figure 11. Histogram of sampled shadow area: from quantized image 1.

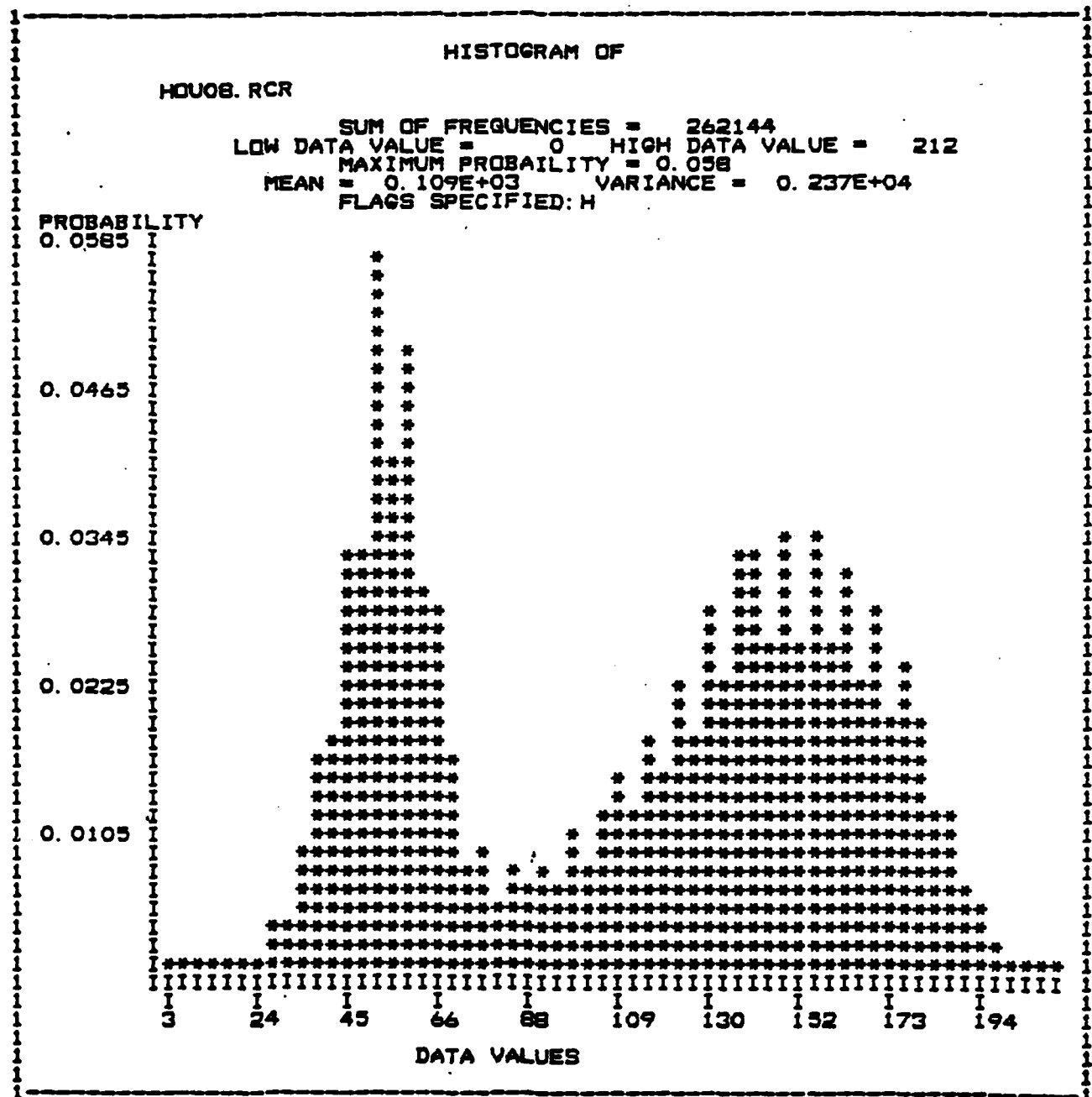


Figure 12. Histogram of texture entropy (q): from the quantized image 1.

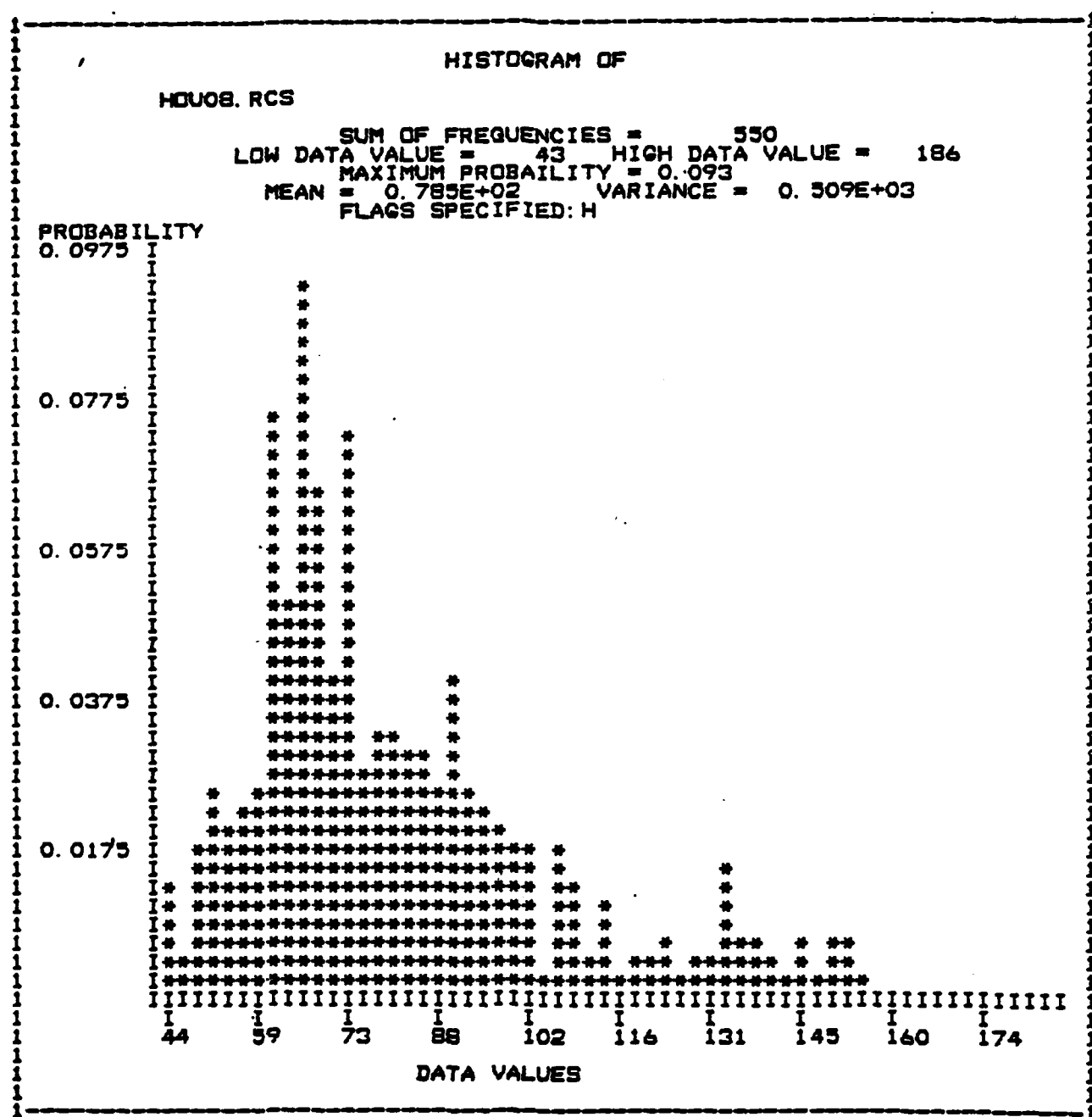


Figure 13. Histogram of texture entropy (s): from sampled shadow area of quantized image 1.

HISTOGRAM OF

HDU08.RCW

SUM OF FREQUENCIES = 5100
LOW DATA VALUE = 4 HIGH DATA VALUE = 82
MAXIMUM PROBABILITY = 0.063
MEAN = 0.479E+02 VARIANCE = 0.131E+03
FLAGS SPECIFIED: H

PROBABILITY
0.0683

0.0543

0.0403

0.0263

0.0123

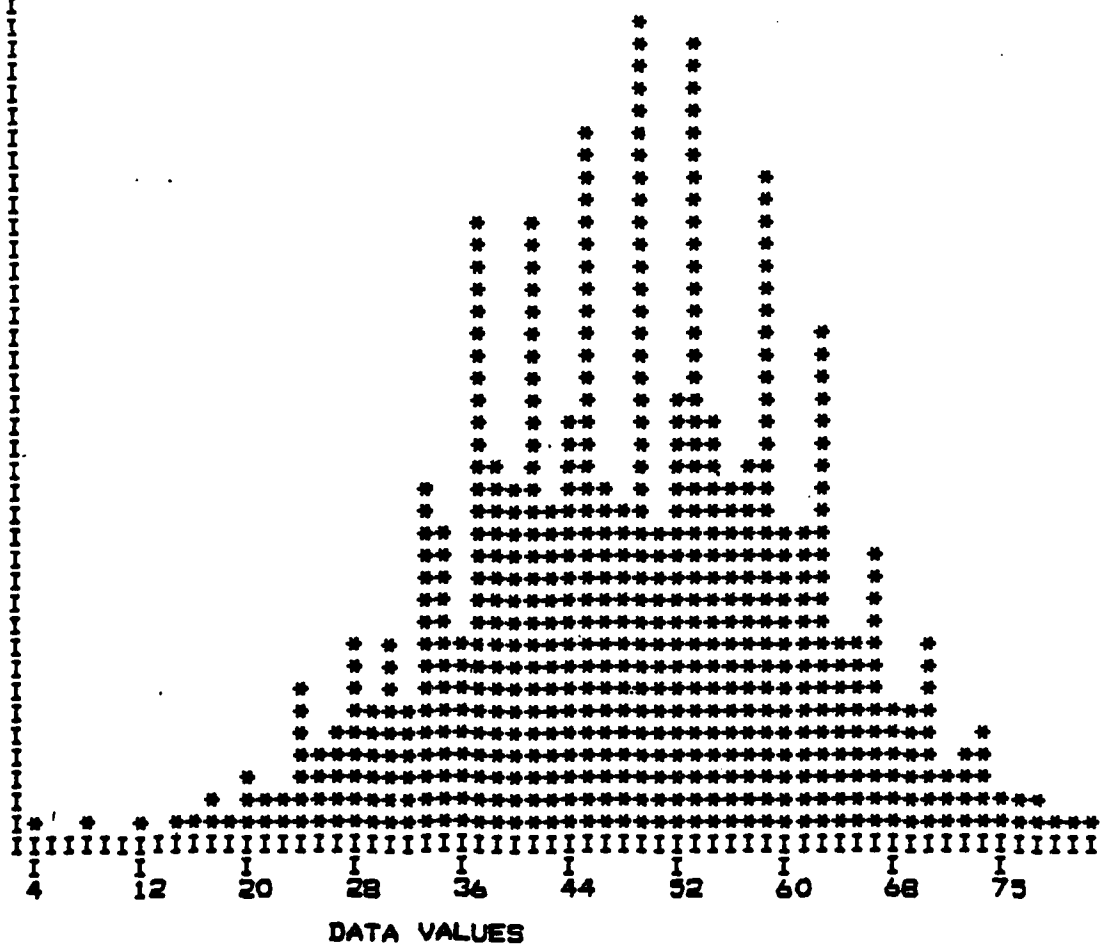


Figure 14. Histogram of texture entropy (w): from sampled water area of quantized image 1.

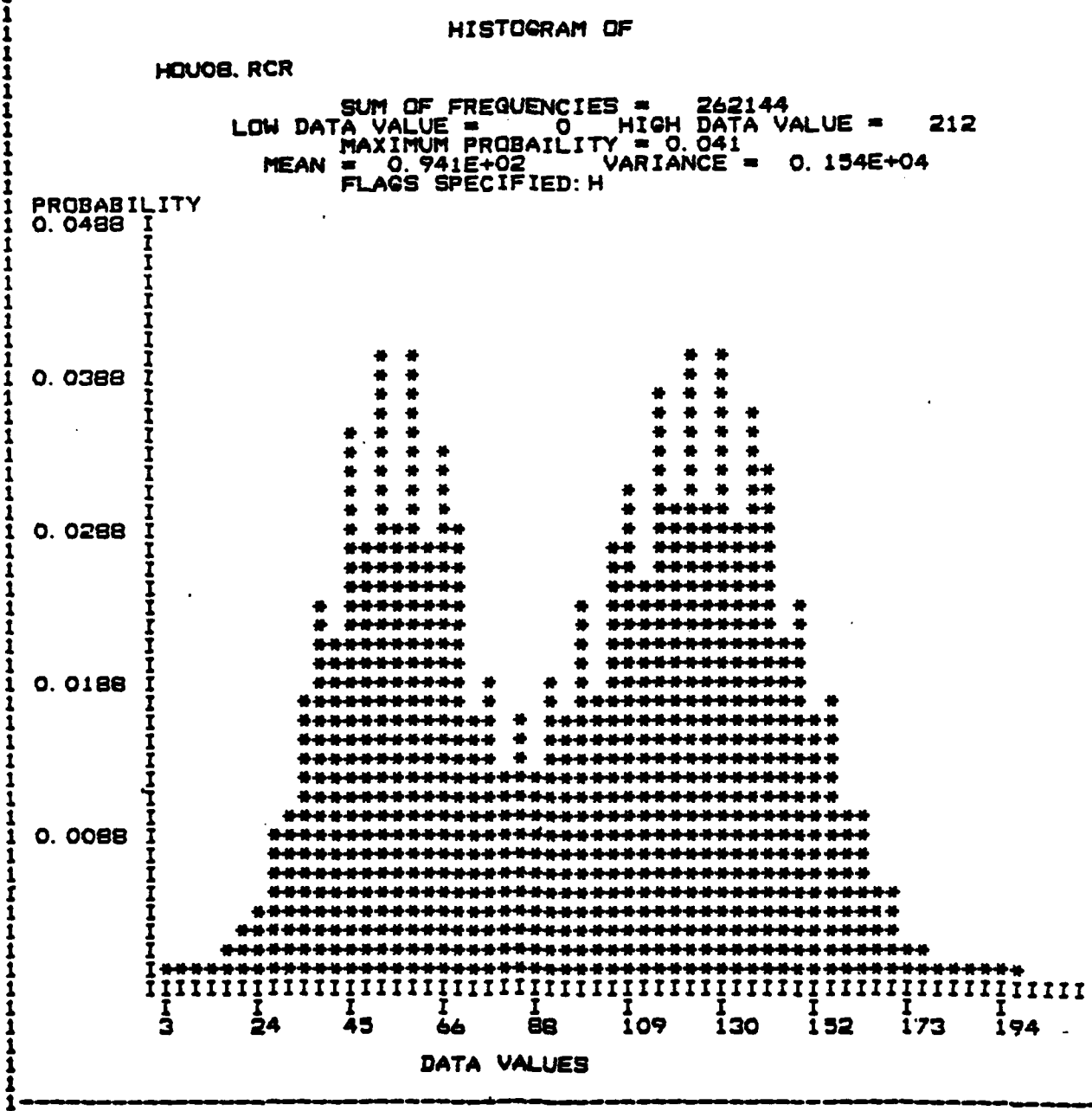


Figure 15. Histogram of inverse difference moment(q): from the quantized image 1.

HISTOGRAM OF
HOUOB. RCW

SUM OF FREQUENCIES = 3100
LOW DATA VALUE = 4 HIGH DATA VALUE = 82
MAXIMUM PROBABILITY = 0. 073
MEAN = 0. 512E+02 VARIANCE = 0. 985E+02
FLAGS SPECIFIED: H

PROBABILITY
0. 0780

0. 0620

0. 0460

0. 0300

0. 0140



Figure 16. Histogram of inverse difference moment (w): from sampled water area of quantized image 1.

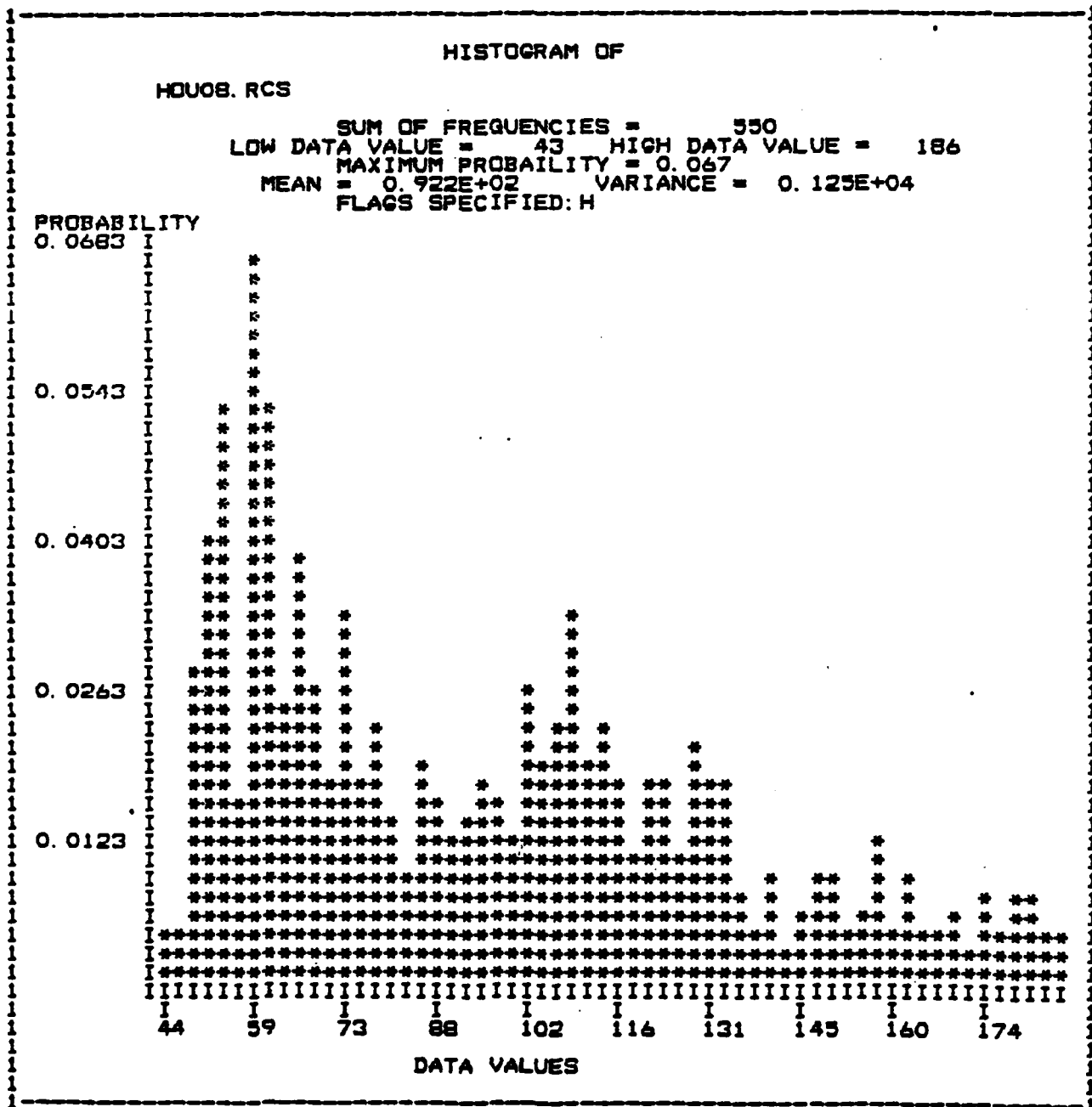


Figure 17. Histogram of inverse different moment (s): from sampled shadow area of quantized image 1

HISTOGRAM OF

HOUQBF. RCR

SUM OF FREQUENCIES = 262144
 LOW DATA VALUE = 0 HIGH DATA VALUE = 209
 MAXIMUM PROBABILITY = 0.214
 MEAN = 0.822E+02 VARIANCE = 0.370E+04
 FLAGS SPECIFIED: H

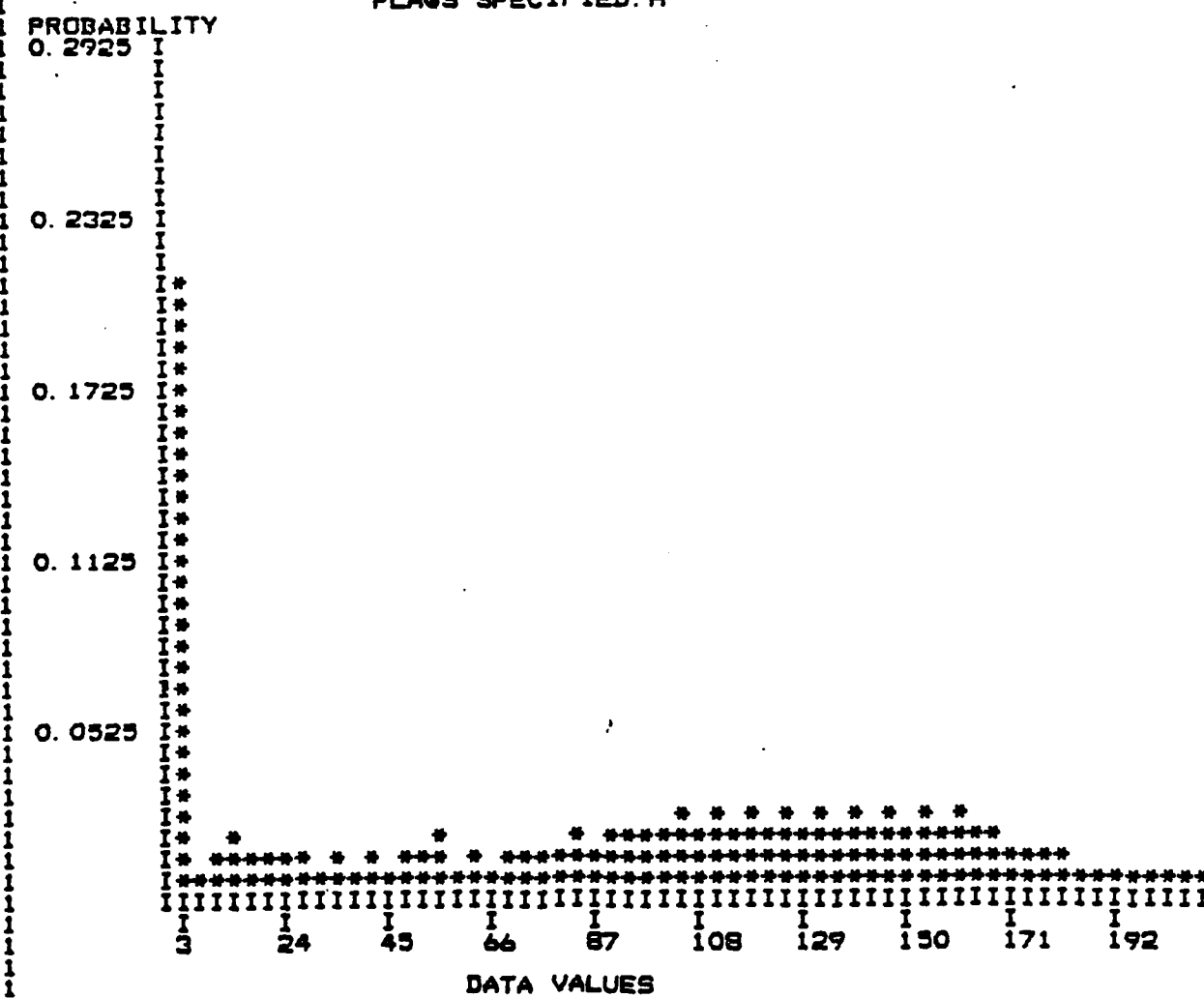


Figure 18. Histogram of entropy (f1): from MTA filtered image 1.

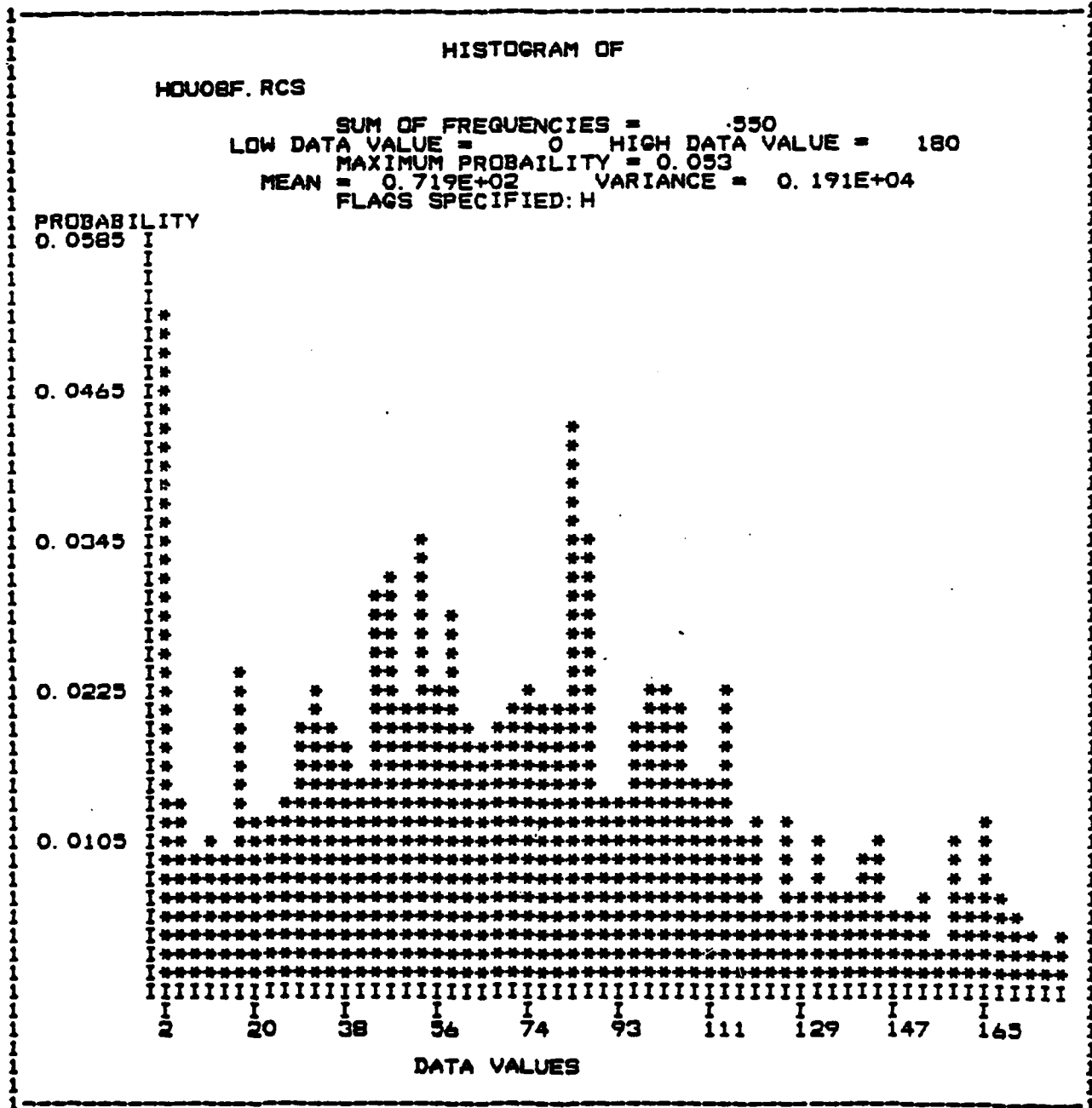


Figure 19. Histogram of entropy (f_2): from sampled shadow area of MTA filtered image 1.

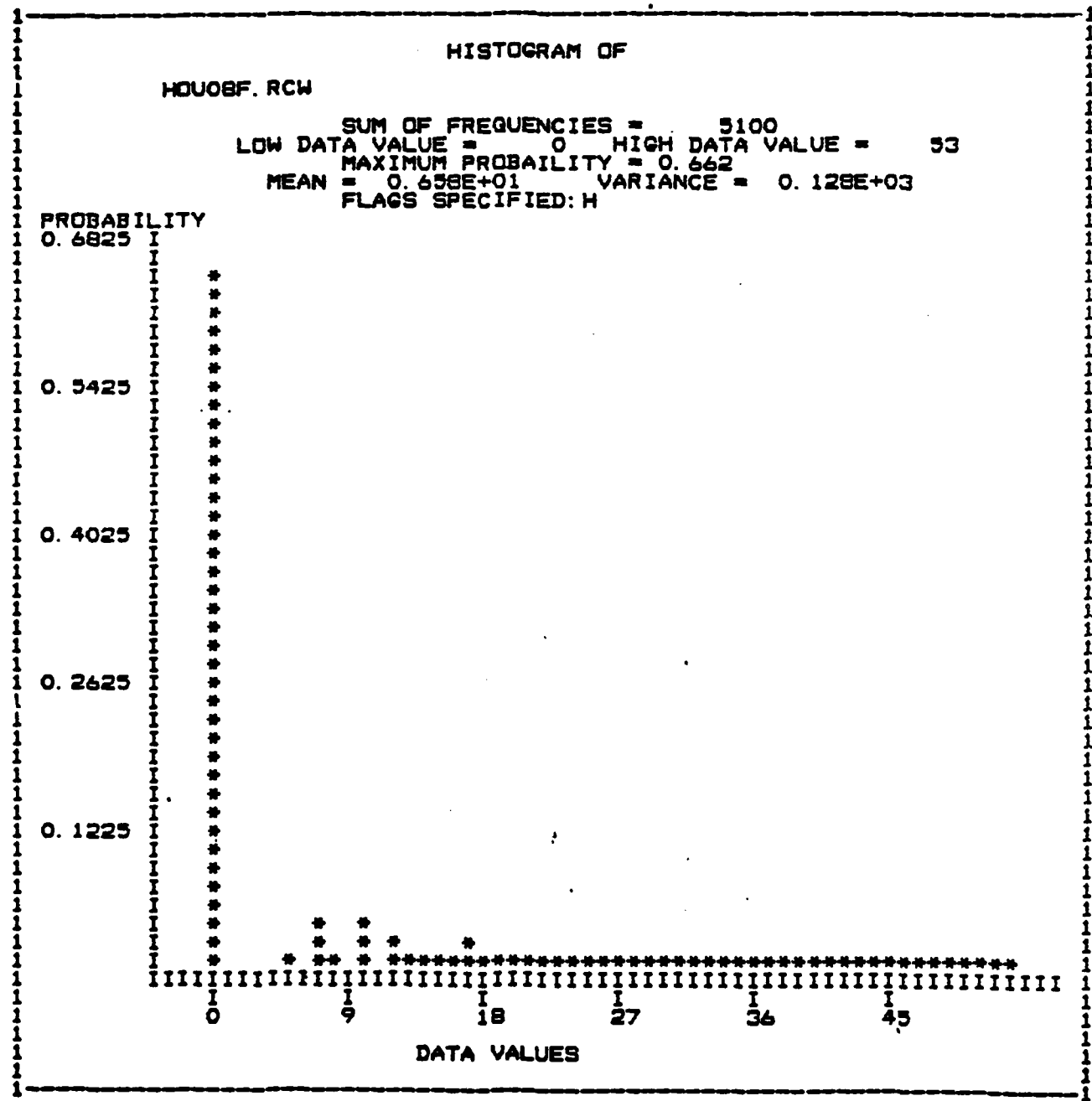
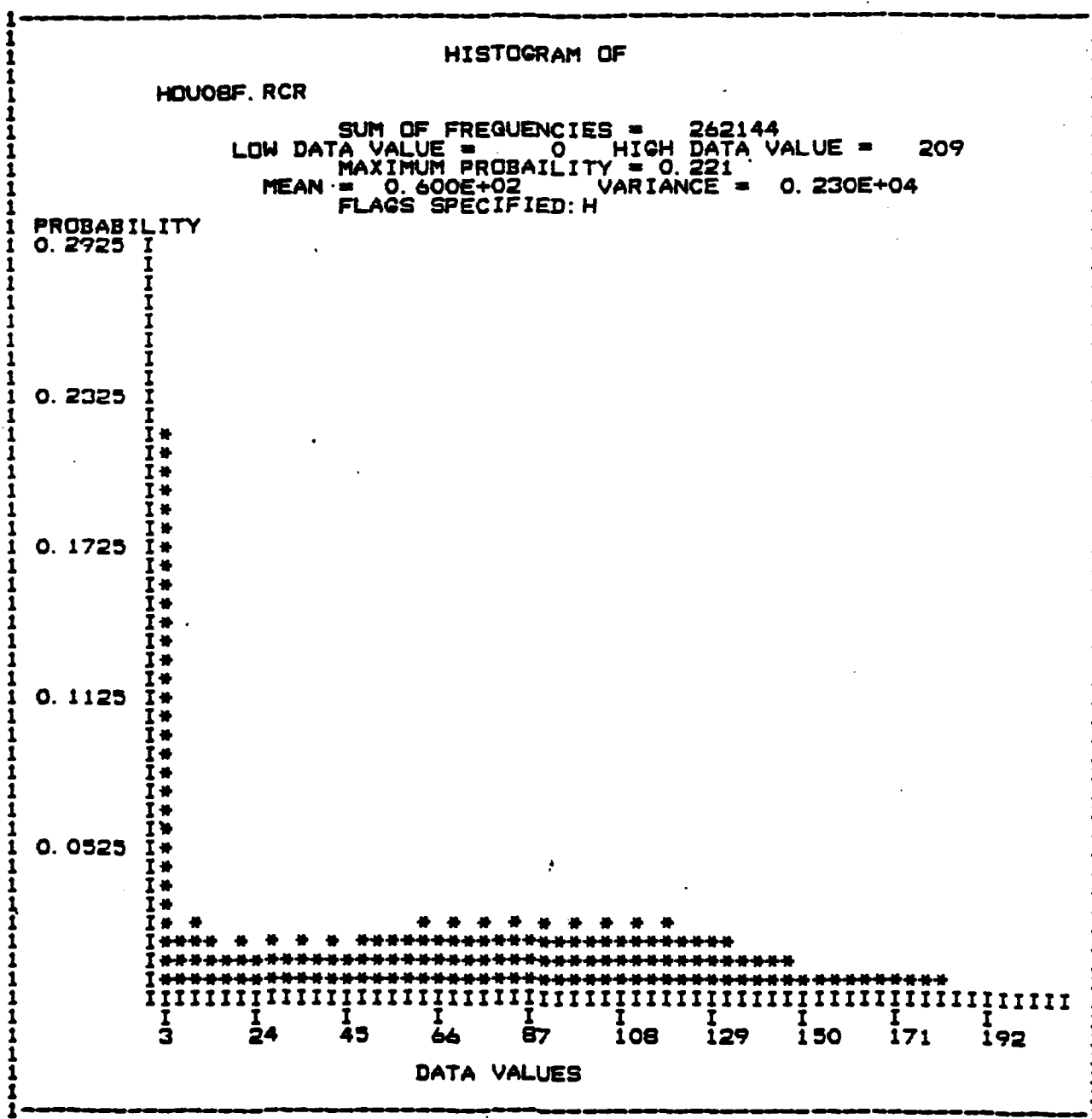


Figure 20. Histogram of entropy (f3): from sampled water area of MTA filtered image 1.



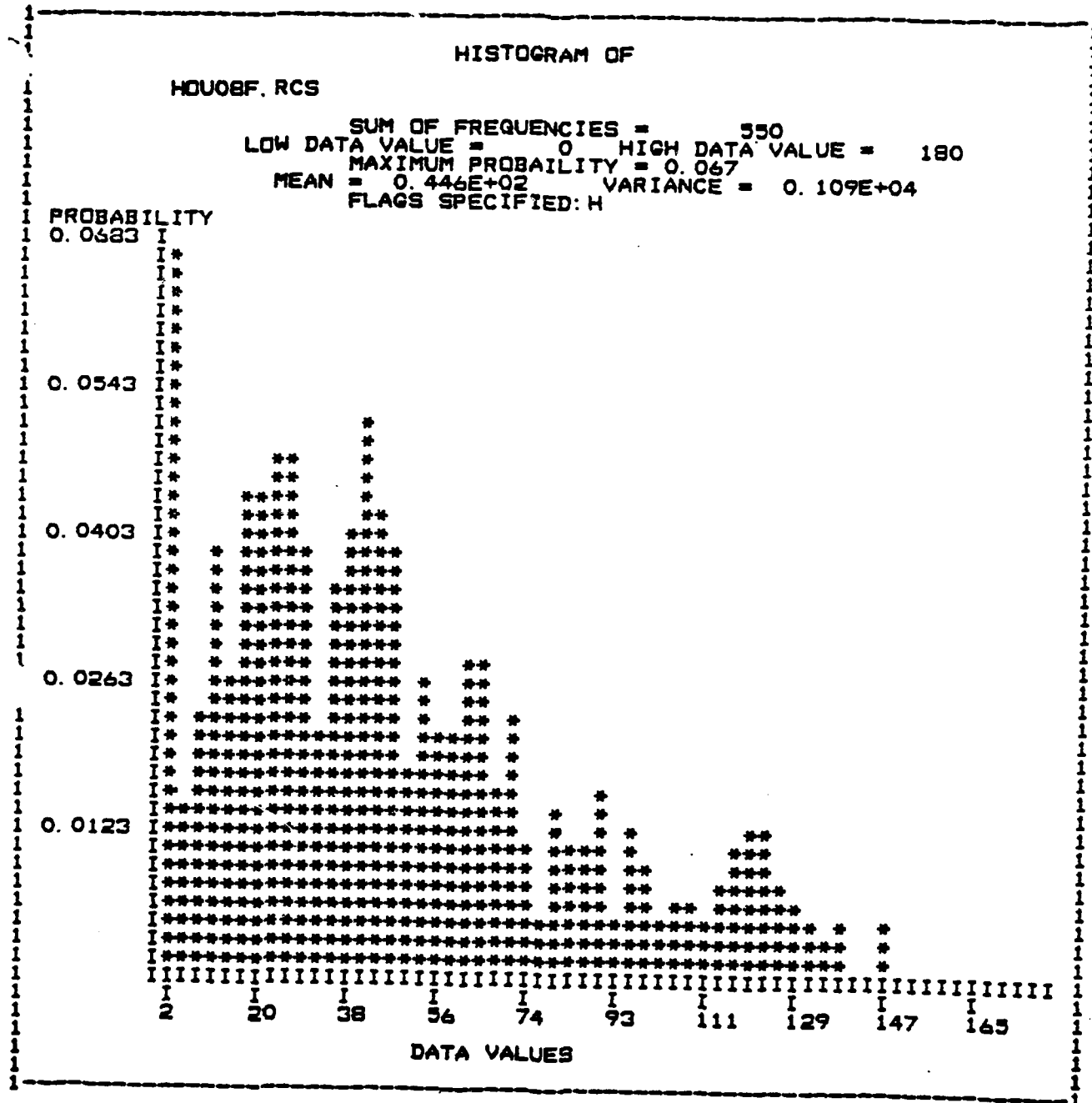


Figure 22. Histogram of inverse difference moment(f2): from sampled shadow area of quantized image 1 .

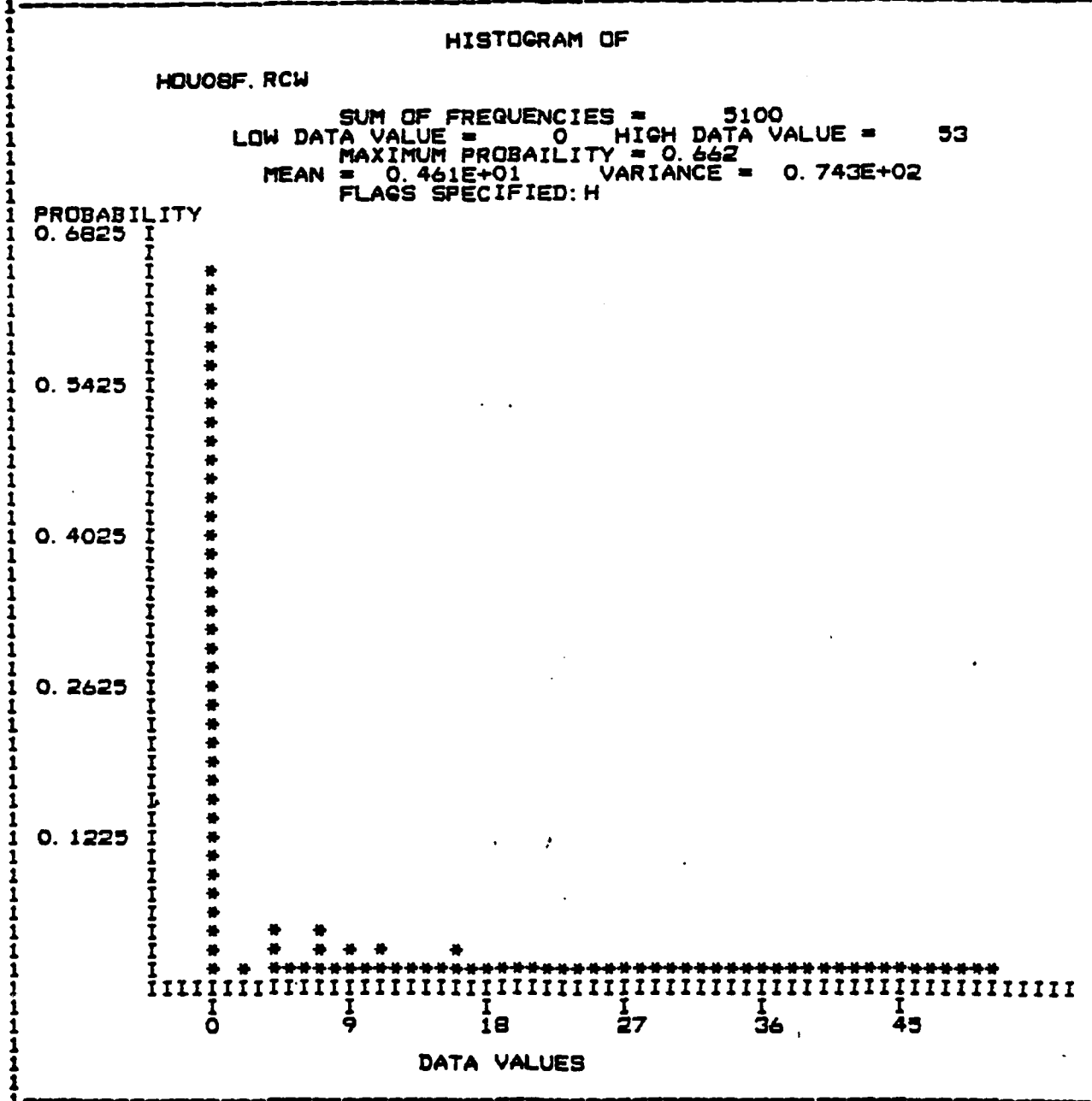


Figure 23. Histogram of inverse difference moment(f_3): from sampled water area of MTA filtered image 1.

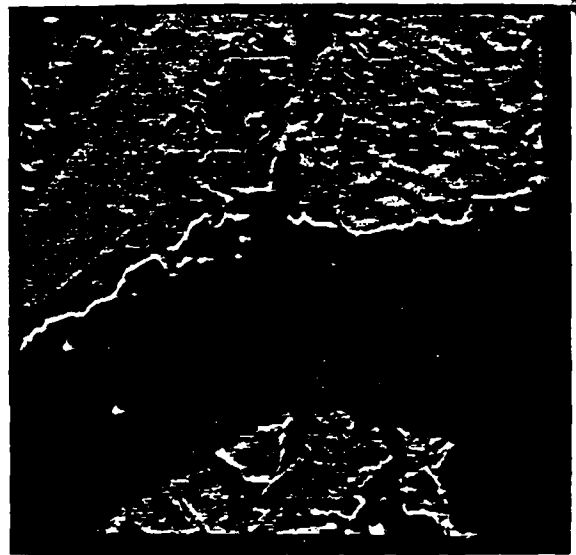


Figure 24. Test image 2: large water body and small shadows on land.

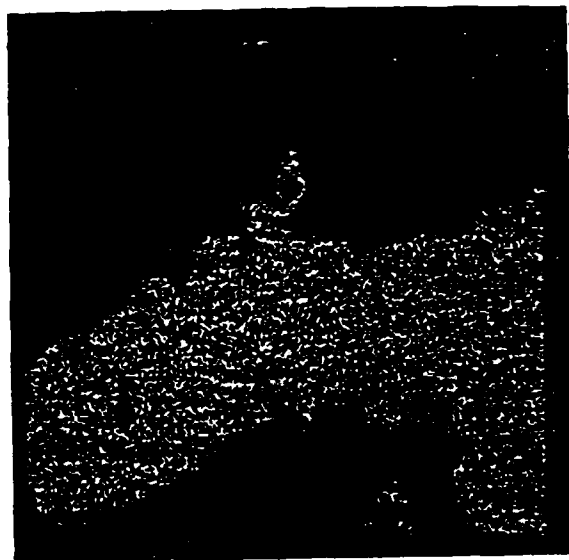


Figure 25. GTCM texture image for image 2.



Figure 26. Segmentation of image 2 (a): shadow regions on land are misclassified as water regions.



Figure 27. Segmentation of image 2 (b): using another set of thresholding values.

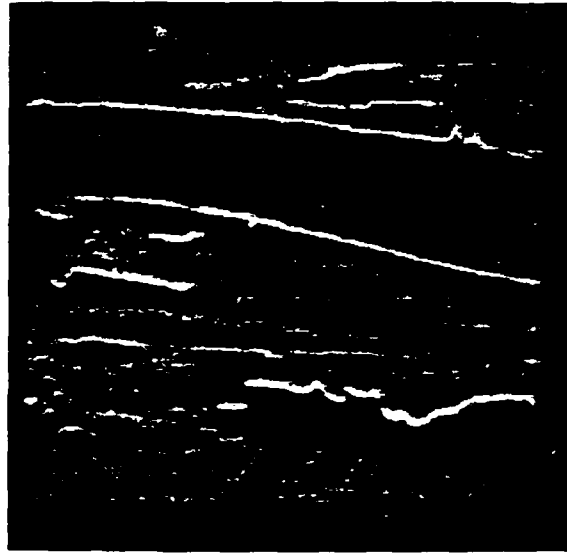


Figure 28. Test image 3: Bright linear features located on region boundaries.

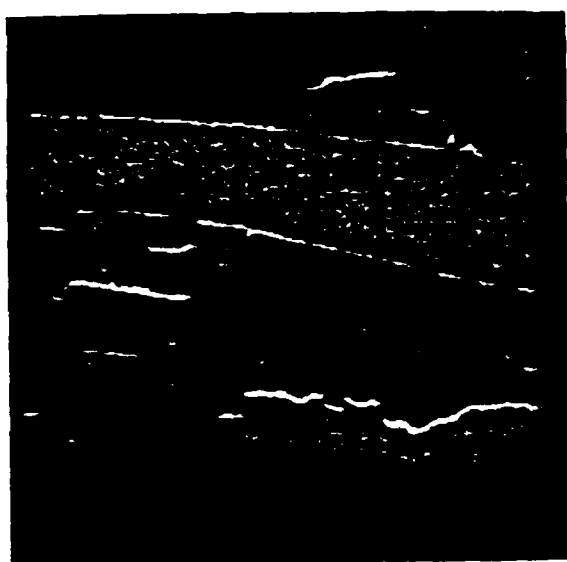


Figure 29. Thresholding GTCM of image 3.

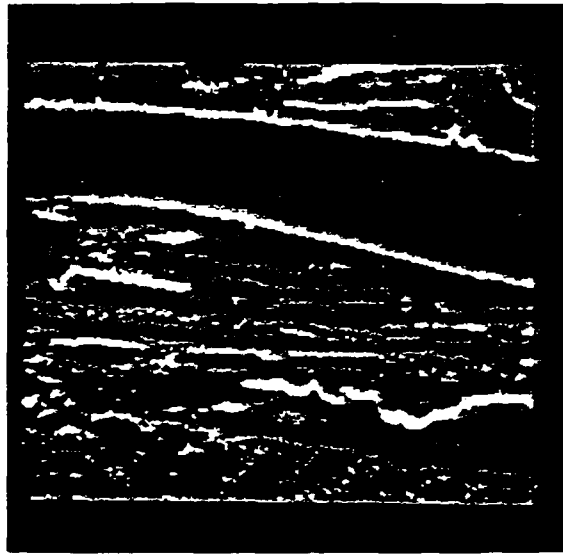


Figure 30. Bright linear features: White- bright linear features, black- possible water and shadows, blue- others.

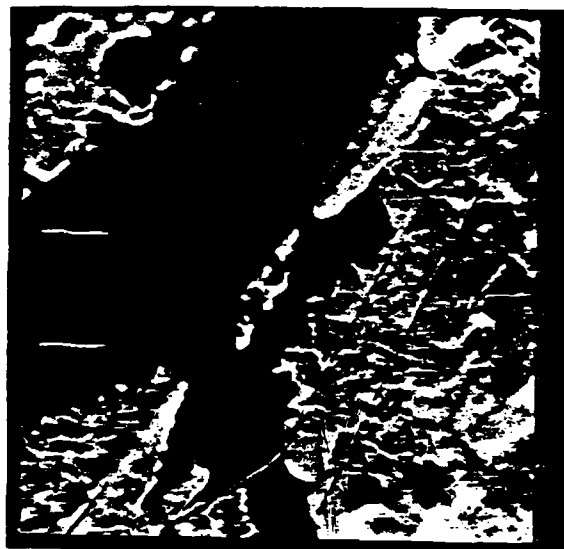


Figure 31. Filtered result of image 1: Filtered by the multi-threshold adaptive filtering.

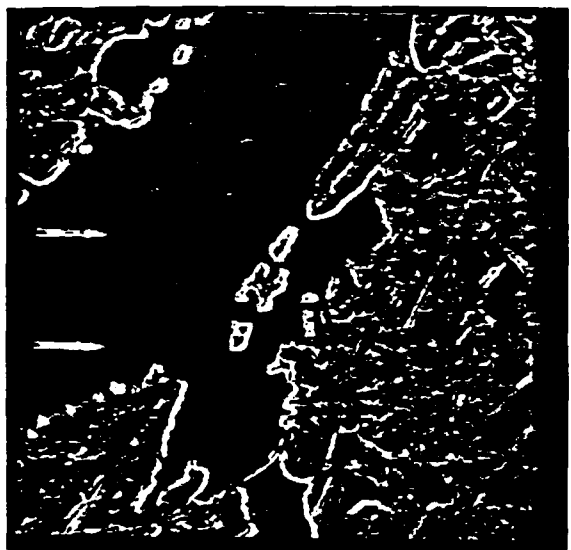


Figure 32. Generalized gradient image (1): Black- for average filter, blue- for sigma filter, red- for weighted edge filter, white- for median filter.

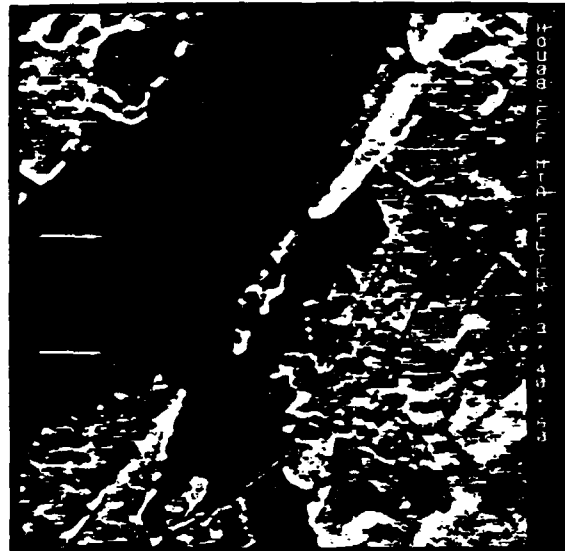


Figure 33. Filtered result by different thresholds: Filter- MTA.

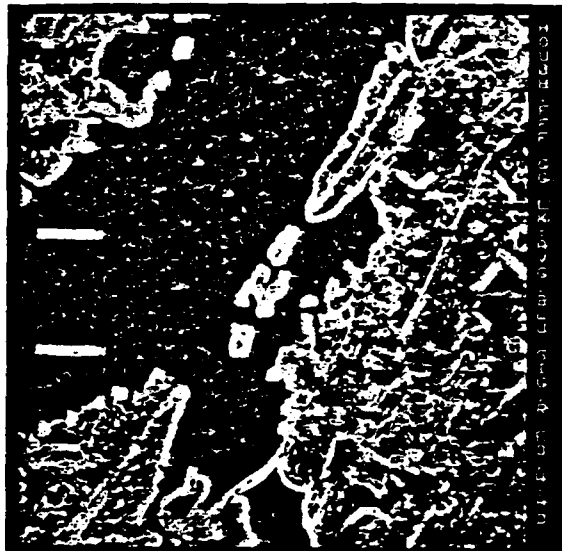


Figure 34. Generalized gradient image (2): Black-for average filter, blue- for sigma filter, red- for weighted edge filter, white- for median filter.

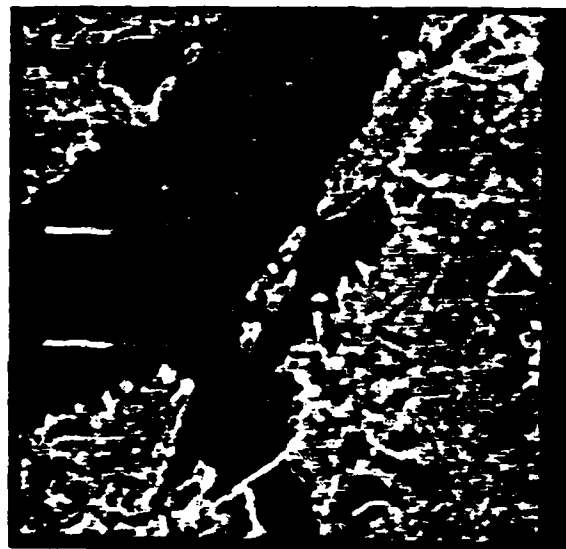


Figure 35. Inverse difference moment image (1): from test image 1, window size= 7 x 7, distance= 2.

RD-A164 912 DISCRIMINATION OF WATER FROM SHADOW REGIONS ON RADAR
IMAGERY USING COMPUTER VISION TECHNIQUES(U) MNEMONICS
INC SALINE MI J QIAN ET AL. SEP 85 ETL-8404

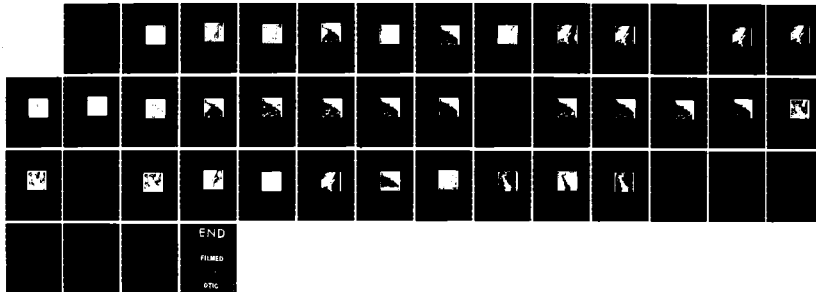
UNCLASSIFIED

DACR76-84-C-0003

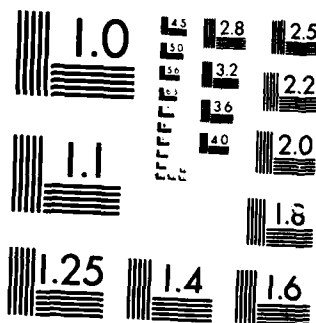
2/2

F/G 17/9

NL



END
FILMED
BY
OTIC



MICROCOPY RESOLUTION TEST CHART
NATIONAL BUREAU OF STANDARDS 1963-A

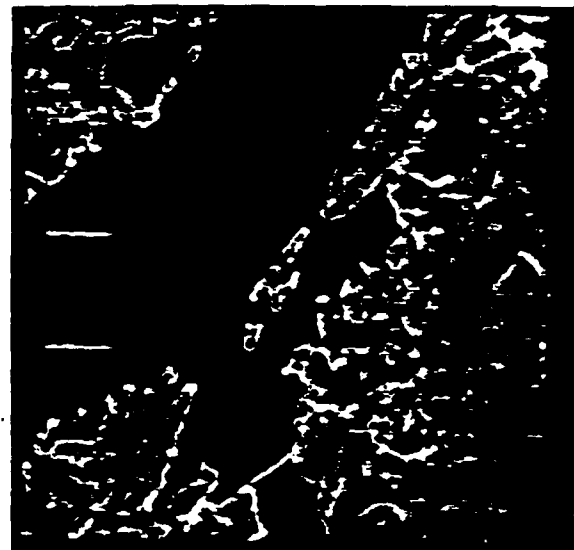


Figure 36. Inverse difference moment image (2): from
MTA filtered image 1, window size= 7 x 7,
distance= 2.

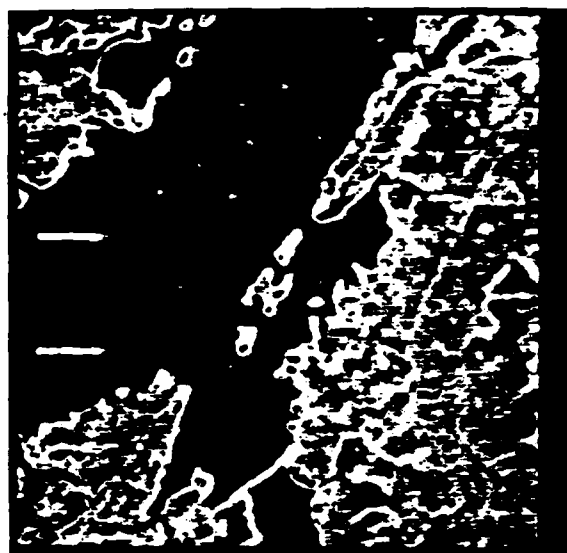


Figure 37. Entropy image of image 1: Window size= 7 x 7, distance= 2.

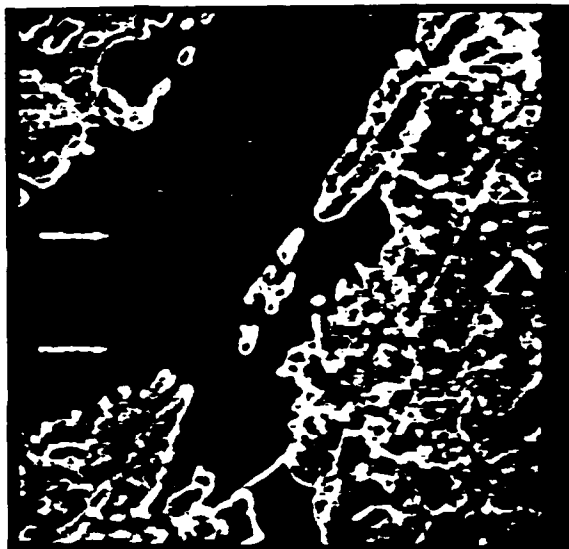


Figure 38. Entropy of filtered image 1: Window size- 7 x 7, distance- 2, filter- MTA.

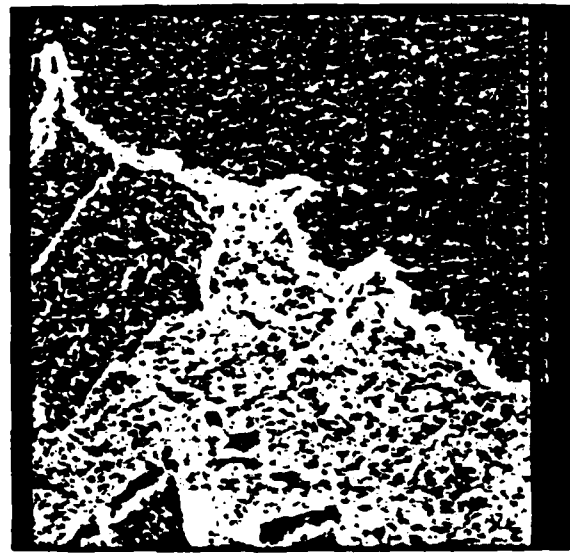


Figure 39. Generalized gradient image (a): from the noisy image with noise $\sigma=10$. Black: for averaging filter. Blue: for Sigma filter. Red: for weighted edge filter. White: for Median filter.

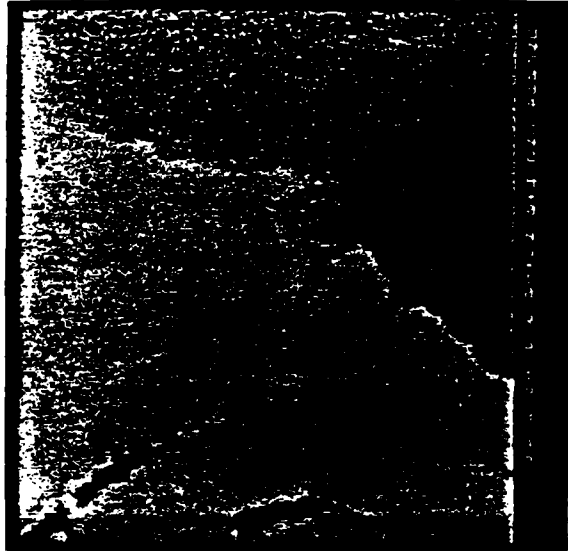


Figure 40. Labeling result (a1): from the noisy image with noise $\sigma=10$. Blue: shadows. Black: water. White: others.



Figure 41. Labeling result (a2): from the corresponding MTA filtered image. Blue: shadows. Black: water. White: others.

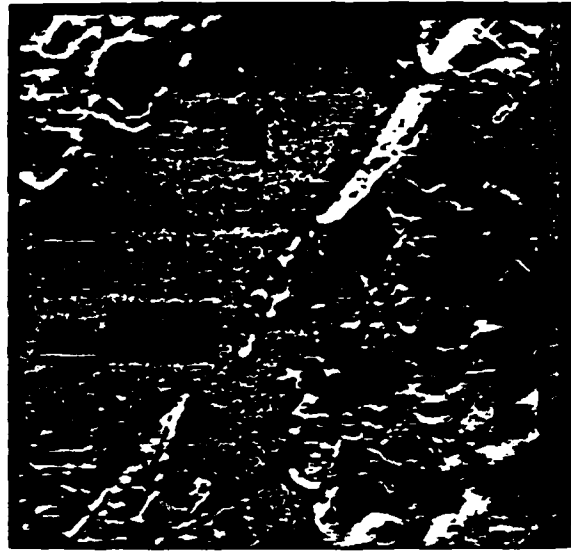


Figure 42. Training sample set for image 1: Brown - water, green - others,Yellow- shadow.

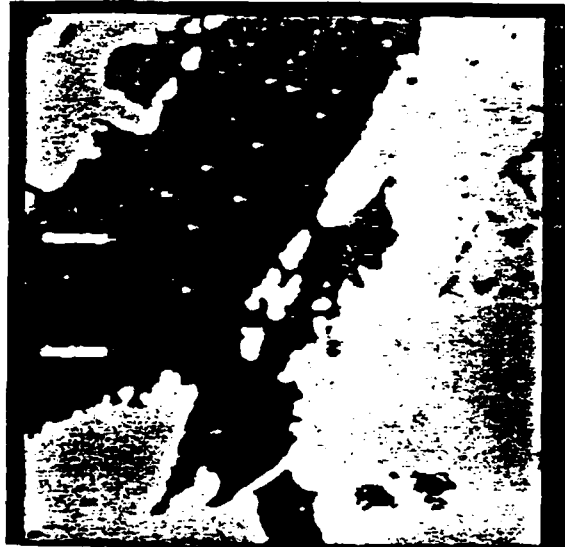


Figure 43. Labeling result for image 1 (a): With texture computed using window size 7×7 , distance 1, key: black-water, blue-shadow and white-others, the classifier is a Gaussian Maximum Likelihood classifier.



Figure 44. Relaxation result for above image: One iteration using Adaptive Relaxation. Black-water, blue-shadow, white-others.

		Water		
		1	2	3
Mean		3.422	77.72	130.3
Covariance		130.3 3.916 -0.3811	0.8443 8.0005	5.837
		Shadow		
		1	2	3
Mean		7.536	125.5	169.3
Covariances		13.36 22.66 273.6	20.49 217.9	178.9
		Others		
		1	2	3
Mean		35.56	150.6	204.4
Covariances		109.7 15.82 248.2	18.63 208.7	186.8

- 1: gray tone
- 2: entropy
- 3: inverse different moment

Figure 45. The mean and covariances for figure 46: estimate from sampling set in fig 42.



Figure 46. Labeling result for image 1 (b): With texture computed using a 12×12 window, distance 6, and Gaussian Maximum likelihood classifier.



Figure 47. Labeling result for image 1 (c): Texture computed using a 20×20 window, Distance 4, and a Gaussian Maximum likelihood classifier.

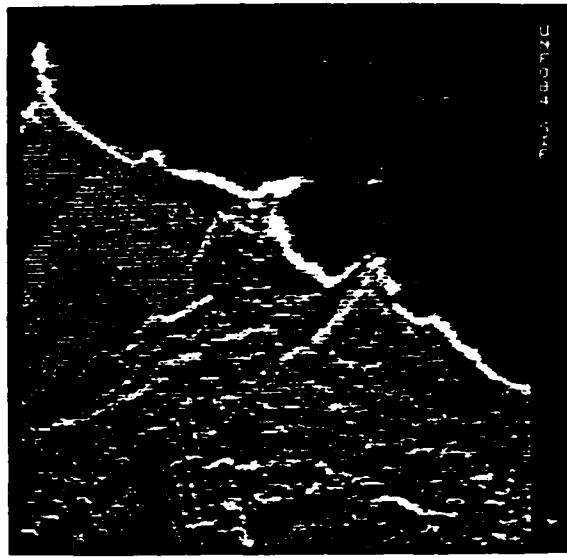


Figure 48. Test image 4.: Large black area -water,
small black regions on land- shadows.

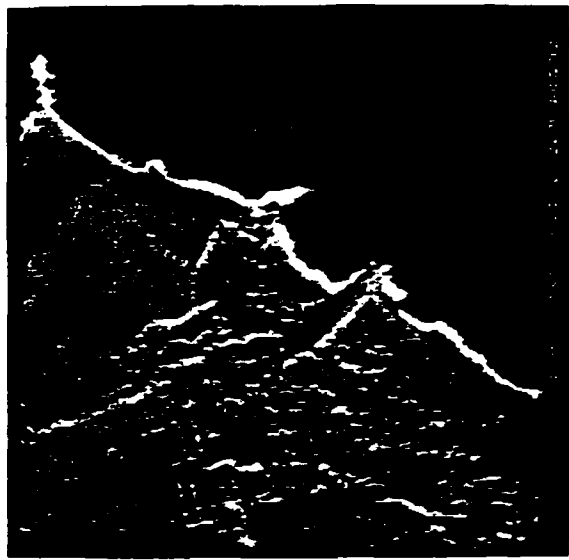


Figure 49. Quantized image 4: quantization level = 128.

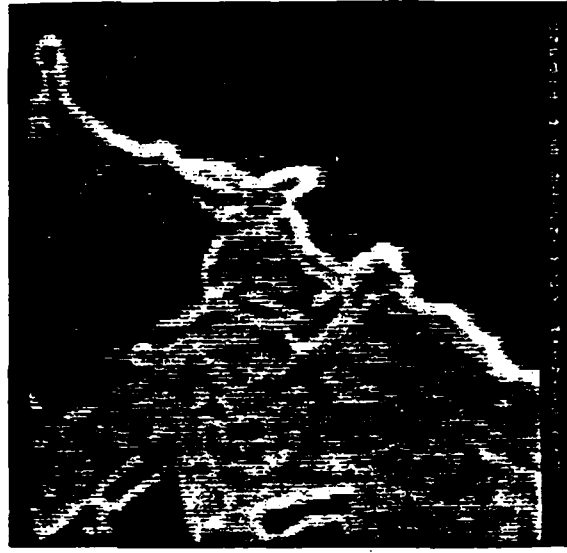


Figure 50. Entropy of image 4: texture computed using a 16x16 window and distance 8.



Figure 51. Inverse different moment of image 4: texture computed using a 16x16 window and distance 8.



Figure 52. Training sampling set for image 4: Green - others, Brown - water, Yellow - shadow.



Figure 53. Labeling result for image 4 (a): texture computed using a 5×5 window and distance 2, labeled by Gaussian Maximum Likelihood classifier, black- water, blue-shadow, white- others.



Figure 54. Labeling result for image 4 (b): texture computed using a 12×12 window and distance 6, labeled by Gaussian ML classifier. Black-water, blue-shadow, white-others.



Figure 55. Labeling result for image 4 (c): texture computed using a 10x10 window and ditance 4, labeled by Gaussian ML classifier, black-water, blue-shadow, white-other.

		Water		
		1	2	3
Mean		16.41	56.83	93.47
Covariances		116.5		
		139.0	226.5	
		338.6	557.5	946.6
		Shadow		
		1	2	3
Mean		25.59	118.6	172.4
Covariances		47.40		
		90.54	108.1	
		770.4	939.6	1161.
		Others		
		1	2	3
Mean		75.67	117.9	173.8
Covariances		130.9		
		-183.7	-194.2	
		636.2	684.7	758.4

- 1: gray tone
- 2: entropy
- 3: inverse difference moment

Figure 56. The mean and covariances for fig. 57: estimate from sampling set in figure 52.

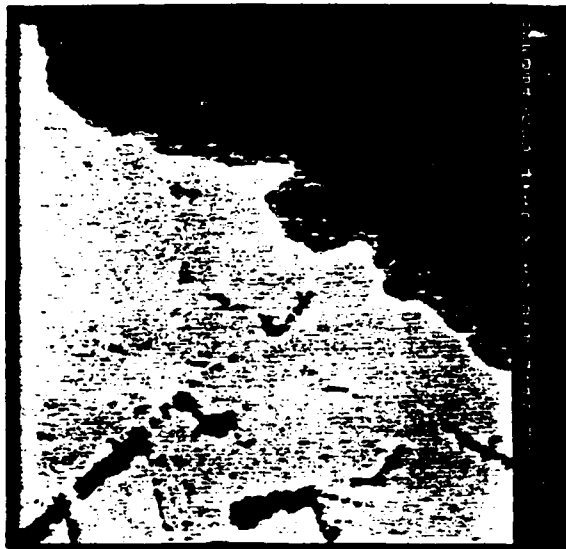


Figure 57. Labeling result for image 4 (d): texture computed using a 16x16 window and distance 8, labeled by Gaussian ML classifier, black-water, blue-shadow, white-other.



Figure 58. Relaxation result for fig. 57 (a): 1 iteration using adaptive relaxation, black-water, blue-shadow, white-other.



Figure 59. Relaxation result for fig. 57 (b): 5 iterations using adaptive relaxation, black-water, blue-shadow, white - others.



Figure 60. Labeling result for image 4 (e): texture computed using a 20×20 window and distance 10, labeled by Gaussian Maximum likelihood classifier, black-water, blue-shadow, white-other.



Figure 61. Initial labeling result: by non-context labeling using Maximum Likelihood decision rule. Image size: 150 x 150.

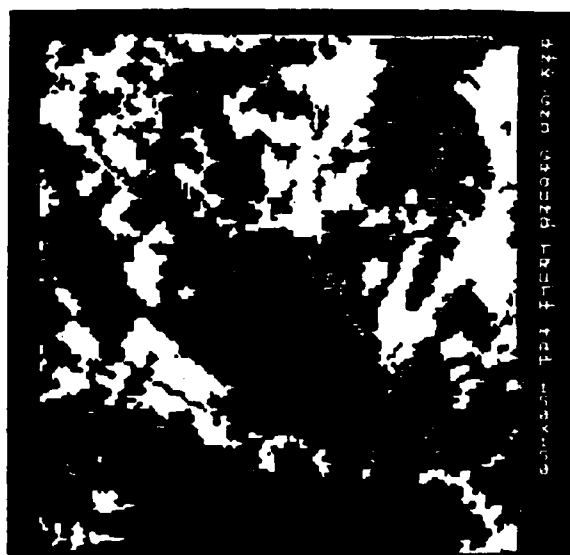


Figure 62. Ground truth map.: Image size: 150 x 150.

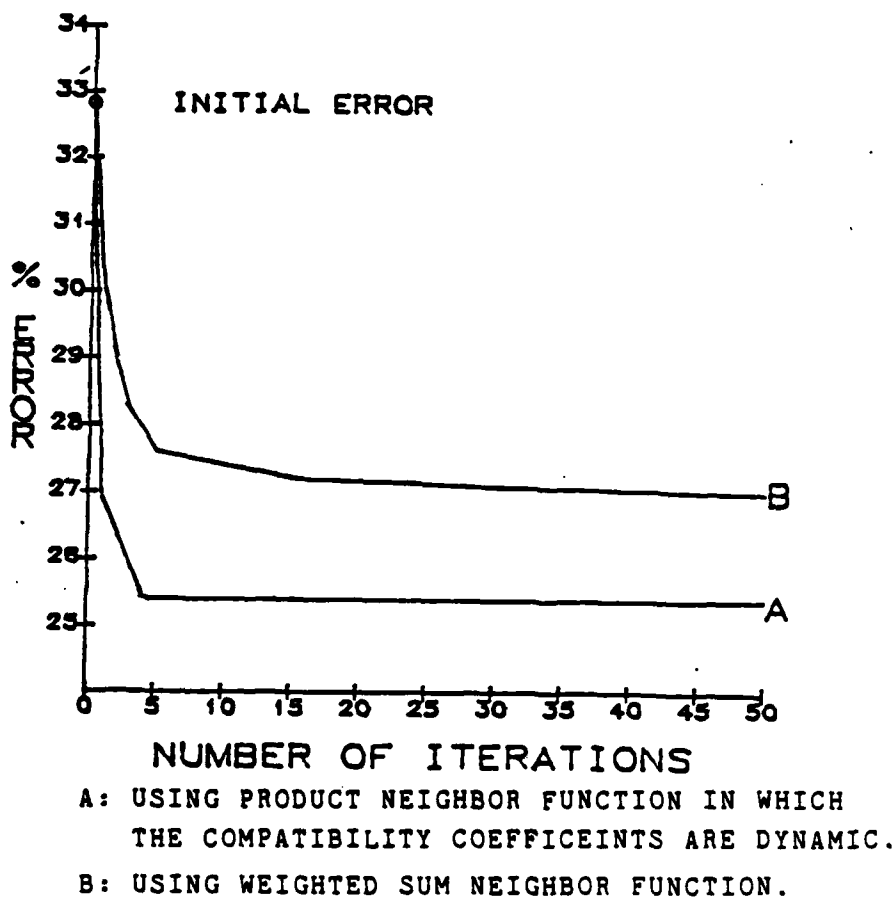


Figure 63. Comparison of error reduction.

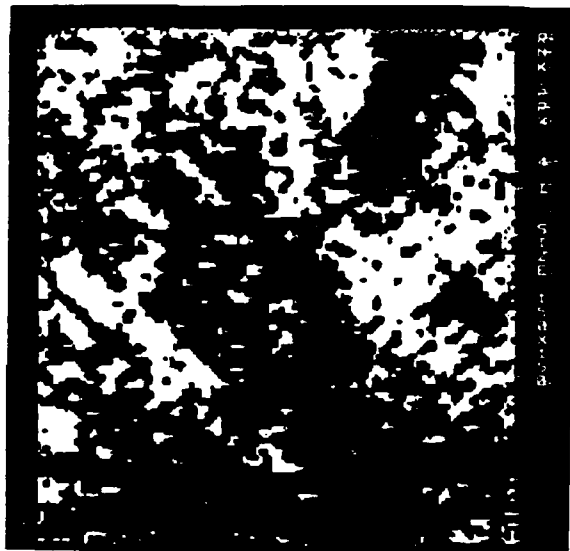


Figure 64. Labeling result: fourth iteration using product neighbor function and dynamic compatibility coefficient. Image size: 150 x 150.



Figure 65. New indexing symbolic image 1.: Region
number=54, categories: water, shadow and
others.

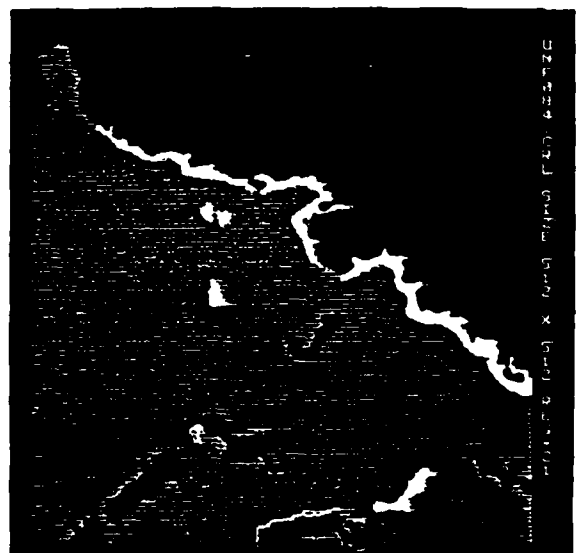


Figure 66. New indexing symbolic image 2.: Region number=21, categories: water, shadow and others.



Figure 67. Spatial reasoning result 1.: Black: water,
Blue: shadow, White: others.



Figure 68. Spatial reasoning result 2.: Black: water,
Blue: shadow, White: others.



Figure 69. Test image 5: Collected in the same condition as test image 4. Image size: 512 x 512, quantization level: 128.

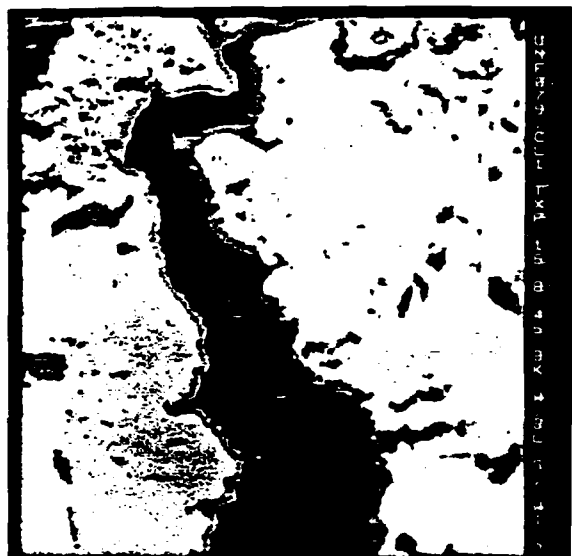


Figure 70. Low level labeling of image 5: mean and covariances estimated from the sampling set in test image 4, labeling method is the same as that for image 4. Black: water, Blue: shadow, White: others.

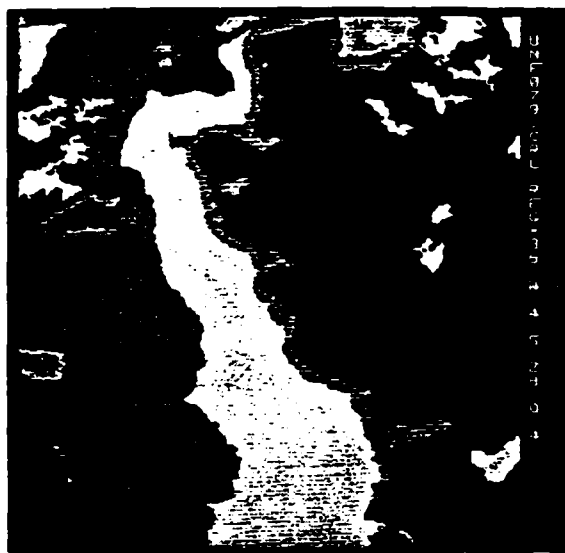


Figure 71. New indexing symbolic image 3: Region
number=36, categories: water, shadow and oth-
ers.



Figure 72. Spatial reasoning result 3: Black: water,
Blue: shadow, White: others.

VII.CONCLUSIONS

We presented a scene analysis system for identifying the shadows and water on SAR image in this report. All experiments done have shown that this system is practical for our purpose. From the final results, we can see that most shadow regions and water regions were identified correctly.

This system was designed so that it used the contextual information sufficiently, wherever in the preprocessing , in the pixel level labeling or in the region level reasoning. In this way, it overcame the specific identification difficulty that the objects to be discriminated were only with subtle differences in tone and texture.

In the preprocessing, we described a region-dependent Multi-Threshold Adaptive filtering technique for texture preserving noise removal. It used a generalized gradient function which reflected the local contextual information as a cue to determine the nature of filtering for each local neighborhood. As a result, a balanced texture preserving and noise removal effect was simultaneously achieved.

In the low-level labeling, we discussed a probabilistic relaxation algorithm in which the adaptive compatibility coefficients were computed by local average estimate and were dynamic in the whole updating process. It extracted most contextual information in pixel level just in the fewest

number of iterations. Results show that it successfully reduced the labeling error in less than 5 iterations and then stabilized. There was no degradation in the entire relaxation process.

In the high-level spatial reasoning, the relational graph model based on our prior knowledge of water and shadow regions on SAR imagery was constructed. The corresponding structural decision rules were derived from the relational model. To measure the contextual information in the region-level, we described a one-pass, depth first boundary tracing procedure using a left first, clockwise directed four neighborhood search technique. Using this method, a property file which contained a list of region attributes and region relations was created. Then a spatial reasoning procedure was performed according to the set of structural decision rules. It reduced the errors and ambiguities resulted from low-level labeling significantly. The most false shadow regions and water regions were identified and corrected.

REFERENCES

1. Maurice W. Long, "Radar Reflectivity of Land and Sea," D.C. Heath and Company, 1975, PP 31-35.
2. Drake, B and R. A. Shuchman et al, "Feasibility of Using Multiplex Star Imagery for Water Resource Management and Mapping Vegetation Communities," Ninth International Symposium on Remote Sensing of Environment, Environmental Research Institute of Michigan, April 15-19, 1974.
3. L. J. Porcello, "Speckle Reduction in Synthetic-aperture Radars," J. Opt. Soc. Amer., Vol.66, No.11, PP 1305-1311, 1976.
4. J. S. Lee, "Digital Image Smoothing and The Sigma Filter," Computer Graphics and Image processing, Vol.24 1983, pp 255-269.
5. J. S. Lee, Refined Filtering of Noise Using Local Statistics, Computer Graphics and Image Processing, 15, 1981, PP 380-389.

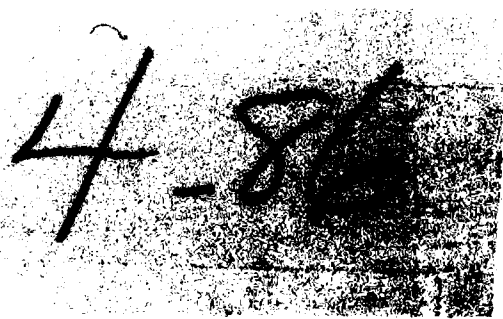
6. G. J. Yang and T. S. Huang, " Median Filters and Their Application to Image Processing," Purdue University, TR -EE 80-1, 1, 1980.
7. R. M. Haralick, K. Shanmugan and I. Dinstein, " Texture Features for Image Classification," IEEE Trans. on Sys. Man and Cyber. Vol. SMC.3, 1973, PP 610- 621.
8. Sam Shanmugan et al., " Texture Features for Radar Image Analysis " IEEE, Trans. on Geoscience and Remote Sensing, Vol.GE. 19 No.3 1981,PP 153-156.
9. R. M. Haralick, " Decision Making in Context," IEEE. Trans. PAMI, VOL. PAMI-5, NO.4, 1983. PP 417-428.
10. Jianzhong Qian and R. M. Haralick, " An Application of Relaxation to Remote Sensing Classification," SDA Lab Technical Report, September 1984.
11. Larry S. Davis and Azriel Rosenfield et al, " Region Extraction by Averaging and Thresholding," IEEE Trans. Sys. Man. and Cyber. May 1975, PP 383-388.
12. R. M. Haralick, "Statistical and Structural Approaches to Textures," in Proc. IEEE. 67, No.5, 1979.

13. L. Van. Gool et. al., "Texture Analysis Anno 1983," Computer Vision, Graphics and Image Proc. 29, 1985, 336-357.
14. B.Julesz, "Experiments in the Visual Perception of Texture," Sci. Amer. No.4, 1975, 2-11.
15. R. W. Connors and C. A. Harlow, "Toward a Structural Textural Analyzer Based on Statistical Methods," Computer Graphics Image Proc. 12, 19880, 224-256.
16. A. Rosenfeld, R.Hummel and S. Zucker, "Scene Labeling by Relaxation Operation," IEEE. Trans. Sys. Man. Cyber. Vol. SMC-6, 1976, 420-433.
17. S. Zucker, E. Krishnamurthy and A. Rosenfeld, "Application Relaxatioon to Line and Curve Enhancement," IEEE. Trans. Comp. Vool. C-26, 1977, 394-403.
18. J. Eklundh, H. Yamamoto and A. Rosenfeld, "A Relaxation Method for Multispectral Pixel Classification," IEEE. Trans. Pattern Analysis and Machine Intelligence, Vol. PAMI-2, No.1 1980, 72-75.
19. J. A. Richards, D. A. Landgrebe and P. H. Swain, "On the Accuracy of Pixel Relaxation Labeling," IEEE. Trans. Sys. Man. and Cyber. Vol. SMC-11, 1981, 303-309.

20. H. M. Kalayeh and D. A. Landgrebe, "Adaptive Relaxation Labeling," IEEE. Trans. Pattern Analysis and Machine Intelligence, Vol. PAMI-6, 1984, 369-372.
21. L. G. Shapiro and R. M. Haralick, "Organization of Relational Models for Scene Analysis," IEEE. Trans. PAMI-4, No. 6, 1982, 595- 602.

END

FILMED



DTIC